International Journal of Hydrogen Energy 292 (2026) 158609

Contents lists available at ScienceDirect

International Journal of Hydrogen Energy

journal homepage: www.elsevier.com/locate/he

First-Principles Investigation of the Structural, Electronic and Optical Properties of TiF_2 and Janus TiFBr Monolayers as Candidate Photocatalysts for Water Splitting

Bourama Djonfaga [a], Murat Sahin [b], Gokhan Surucu [c,*]

[a] Graduate School of Natural and Applied Sciences, Gazi University, Ankara, 06500, Türkiye
[b] Mechanical Engineering Department, National Defence University, Ankara, Türkiye
[c] Department of Energy Systems Engineering, Faculty of Technology, Gazi University, Ankara, 06500, Türkiye

ARTICLE INFO

Keywords:
Solar Hydrogen Production
Janus TiFBr Monolayer
Photocatalytic Water Splitting
Density Functional Theory
pH-Dependent Band Alignment
Solar-To-Hydrogen Efficiency

ABSTRACT

First-principles calculations assess the TiF_2 monolayer and its Janus derivative TiFBr as candidate photocatalysts for water splitting. Both adopt the 1H structure, satisfy the elastic stability criteria and remain intact during 10 ps molecular dynamics at 300 K in vacuum; their phonon spectra show only small residual imaginary frequencies near Γ. HSE06 gives gaps of 2.08 eV (indirect, TiF_2) and 1.45 eV (direct, TiFBr). With overpotential allowances of 0.2 and 0.6 eV for hydrogen and oxygen evolution, the band edges of TiF_2 satisfy both allowances only between pH 4.7 and 5.6, where its ideal solar-to-hydrogen efficiency limit is 15.8%. TiFBr does not meet the oxygen-evolution allowance below pH ~ 12, but its out-of-plane dipole raises its conduction band on the Br-terminated side, favouring hydrogen evolution. Scissor-corrected absorption peaks lie in the visible range (about 2.8 and 1.8 eV). Aqueous stability of these Ti^{2+} compounds remains the main open question.

1. Introduction

Hydrogen is central to the decarbonisation of sectors that resist direct electrification, including steelmaking, ammonia synthesis, and heavy transport. Most of today's hydrogen is still produced from fossil fuels, mainly by natural-gas reforming and coal gasification, with substantial CO_2 emissions, so the environmental case for hydrogen depends entirely on how it is made [1,2]. Photocatalytic water splitting offers a route that requires only sunlight, water, and a semiconductor, with no external bias and no carbon feedstock, and it remains attractive for decentralised production because a particulate photocatalyst suspension avoids the balance-of-plant cost of electrolysers [3].

Realising this promise depends on the photocatalyst. A viable candidate must satisfy several requirements at once: a band gap wide enough to drive the 1.23 eV water-splitting reaction but narrow enough to harvest visible photons, band edges that straddle both the hydrogen and oxygen evolution potentials, strong optical absorption, efficient separation of photogenerated carriers, and chemical stability in the operating electrolyte [4,5]. Few materials meet all of them simultaneously, which is why solar-to-hydrogen (STH) efficiencies for particulate systems remain well below the 10% threshold generally regarded as the commercial target [6,7]. The most efficient particulate photocatalysts combine a light absorber with separate cocatalysts that carry out the hydrogen and oxygen evolution reactions [8,9], so the intrinsic properties of the absorber, namely its band gap, band-edge positions, optical absorption and stability, are the first criteria used to screen new candidates [10].

The discovery of graphene and the subsequent growth of two-dimensional (2D) materials expanded the design space for next-generation photocatalysts [11,12]. The large surface-to-volume ratio of monolayers maximises active-site density [13], while quantum confinement and symmetry breaking can be used to tune the band gap [14]. Transition-metal dihalide monolayers of the form MX_2 (M = transition metal, X = halogen) are promising in this respect: the strong electronegativity of halogen atoms widens the band gap and shifts band edges toward water redox levels. Titanium-based systems stand out because Ti is earth-abundant, low in toxicity, and bulk TiO_2 already has a well-established record in photocatalysis [15].

Titanium dihalides have recently attracted attention in this context. Bulk $TiCl_2$, $TiBr_2$ and TiI_2 are known layered compounds [16], and their monolayers have been examined in high-throughput and dedicated first-principles studies [17–19]. Because Ti^{2+} has a d^2 configuration, the

* Corresponding author.
E-mail address: gokhansurucu@gazi.edu.tr (G. Surucu).

https://doi.org/10.1016/j.ijhydene.2026.158609
Received 11 September 2026; Received in revised form 30 October 2026; Accepted 9 November 2026
0360-3199/© 2026 Hydrogen Energy Publications LLC. Published by Elsevier Ltd. All rights are reserved, including those for text and data mining, AI training, and similar technologies.

ground state depends on the coordination: octahedral (1T) layers tend to order magnetically [20], whereas in the trigonal-prismatic 1H phase the 2 d electrons fill an isolated band and the layers are non-magnetic semiconductors [17,19,21]. Recent work has reported TMD-like valley excitons in 1H-$TiBr_2$ [21], defect-controlled reactivity of its basal plane [22] and bright ground-state excitons in 1H-TiI_2 [23]. Janus TiXY monolayers (X, Y═Cl, Br, I) have been predicted to be dynamically stable, non-magnetic semiconductors with HSE06 gaps of 0.83–1.23 eV, tunable Berry curvature and piezoelectric response [24,25]. None of these studies assessed the band edges against the water redox potentials, and the valence-band maxima of 1H-$TiBr_2$ and Janus TiBrI lie near −3.6 and −3.4 eV with respect to vacuum [17,18], far above the O_2/H_2O level (−5.67 eV), so the Cl-, Br- and I-based members of the family are unsuitable for oxygen evolution.

Fluorine, the most electronegative element, offers a route to deeper band edges. For the TiF_2 monolayer, the 1H structure is the lowest-energy polymorph, lying below the 1T′ and 1T forms and even below fluorite-type bulk TiF_2 at the PBE level [26]; it has also appeared in a study of excitons in 1H-TiX_2 [23] and, recently, as one of several monolayers combined with polar Al_2O_3 in van der Waals heterostructures designed for photocatalytic overall water splitting [27]. To our knowledge, however, a detailed assessment of the free-standing monolayer, including its pH-dependent band alignment, overpotential-limited operating window and AM1.5G-weighted absorption, has not been reported. Substituting one fluorine layer with bromine creates the Janus monolayer TiFBr, which lacks out-of-plane mirror symmetry and therefore carries an intrinsic dipole and an internal electric field [28,29]. Such built-in fields can drive photogenerated electrons and holes toward opposite surfaces and relax the band-gap requirement for overall water splitting [30,31]. To the best of our knowledge, no F-containing Janus Ti dihalide, including TiFBr, has been reported; the existing high-throughput Janus data sets include only Cl, Br and I among the halogens [18,29]. Here we characterise TiF_2 and Janus TiFBr with density functional theory, covering structural optimisation, mechanical, dynamical and thermal stability, electronic structure, pH-resolved band-edge alignment, overpotential-limited operating windows, theoretical solar-to-hydrogen efficiencies and optical response, and we compare what each monolayer offers for solar hydrogen production.

2. Computational Methods

All calculations were performed with the Vienna Ab initio Simulation Package (VASP) [32,33] within the generalised gradient approximation (GGA), using the Perdew–Burke–Ernzerhof (PBE) exchange-correlation functional [34] and projector augmented-wave (PAW) pseudopotentials [35,36]. Structural optimisation used a plane-wave cutoff of 530 eV and a 15 × 15 × 1 Monkhorst–Pack k-point mesh, with convergence thresholds of 10^{-7} eV per unit cell for total energy and 10^{-6} eV/Å for atomic forces. A 15 Å vacuum layer was inserted perpendicular to the monolayer plane to minimise interactions between periodic images, giving a cell height of about 18 Å. Calculations were performed without spin polarisation and without spin–orbit coupling (SOC). This choice is motivated by the electronic structure of the trigonal-prismatic 1H phase: the two Ti 3d electrons of Ti^{2+} fill an isolated band that is separated from the empty d states by a gap of about 1 eV already at the PBE level (1.24 and 0.98 eV; Section 3.2), which is consistent with a non-magnetic ground state, as found in spin-polarised studies of the related 1H-TiX_2 (X = Cl, Br, I) and Janus TiXY monolayers [19,25,29]. Spin-polarised test calculations were not performed for the fluorides. SOC was neglected because both band edges are dominated by states of the light element Ti (Fig. S2); its effect, expected to be small, was not quantified. No dipole correction was applied; its effect on the Janus layer is quantified in Section 3.2. The main computational parameters are listed in Table 1.

Mechanical stability was evaluated from elastic constants calculated with the ELASTOOL code [37,38]. To verify dynamical stability, phonon dispersions were obtained in Phonopy from finite atomic displacements imposed on a 4 × 4 × 1 supercell [39,40]. Behaviour at 300 K was then probed through molecular dynamics (MD) runs of 10 ps carried out in VASP [32]; because ab initio MD is computationally expensive, machine-learned force fields (MLFF) trained on the fly against PBE reference calculations were used to reduce the cost [41,42]. These MLFF-MD runs used a Langevin thermostat on a 4 × 4 × 1 supercell containing 48 atoms.

Table 1
Computational parameters used in this work.

Quantity	Setting
Code, method	VASP, PAW pseudopotentials, PBE (GGA)
PAW datasets	PAW_PBE Ti, F and Br (standard VASP datasets)
Plane-wave cutoff	530 eV
k-point mesh (PBE relaxation)	15 × 15 × 1 (Monkhorst–Pack)
Convergence (energy/forces)	10^{-7} eV/10^{-6} eV Å^{-1}
Vacuum/cell height	15 Å/≈18 Å
Spin polarisation, SOC	not included (non-magnetic 1H phase)
Dipole correction	not applied (effect estimated in Section 3.2)
Hybrid functional	HSE06, 25% exact exchange, μ = 0.2 Å^{-1}; k-mesh 9 × 9 × 1
Elastic constants	ELASTOOL
Phonons	Phonopy, finite displacements of 0.01 Å, 4 × 4 × 1 supercell, k-mesh 4 × 4 × 1
MLFF-MD	4 × 4 × 1 supercell (48 atoms), 300 K, Langevin thermostat (friction coefficients of 10, 5 and 12 ps^{-1} for Ti, F and Br), time step 1.0 fs, 10 ps, on-the-fly training against PBE, k-mesh 3 × 3 × 1
Optical spectra	PBE, independent-particle approximation; k-mesh 15 × 15 × 1, 30 bands, Lorentzian broadening 0.1 eV; scissor Δ = 0.84 eV (TiF_2), 0.47 eV (TiFBr)
STH efficiency	Fu et al. method, AM1.5G (ASTM G173-03)

Because PBE underestimates band gaps, the screened hybrid HSE06 functional was used for electronic properties [43,44], with 25% exact Hartree–Fock exchange and a screening parameter of 0.2 Å^{-1}. Band-edge positions were referenced to the vacuum level obtained from the planar-averaged electrostatic potential of the same calculation, determined separately for PBE and HSE06; for the Janus layer, the potential adjacent to the F-terminated face was used (Section 3.2). Band structures were visualised with the Sumo toolkit [45], and crystal structures were rendered in VESTA [46].

Linear optical spectra were calculated from the PBE electronic structure in the independent-particle approximation as implemented in VASP [47] and converted into the absorptance, reflectance and transmittance of the free-standing layer as described in Section 3.3 [48,49]. To correct for the PBE gap underestimation, the computed spectra were additionally corrected a posteriori with a scissor operator, which, when the momentum matrix elements are renormalised consistently, amounts to a rigid shift of $\varepsilon_2(\omega)$ by $\Delta = E_g^{HSE06} - E_g^{PBE}$ [50,51]. Excitonic effects were not included. Theoretical solar-to-hydrogen efficiency limits were evaluated with the method of Fu et al. [31], which has been applied to several Janus monolayers [52], using the AM1.5G reference spectrum [53]; the corresponding equations are given in Section 3.4.

3. Results and Discussion

3.1. Structural and Stability Analysis

TiF_2 and Janus TiFBr both adopt the trigonal-prismatic 1H structure, in which each Ti atom is coordinated by three halogen atoms above and three below the metal plane, with the two halogen layers eclipsed when viewed along the surface normal (Fig. 1). In TiF_2, fluorine atoms occupy both the top and bottom planes, giving a symmetric F–Ti–F configuration with space group P-6m2 (No. 187, point group D_3h), which contains a horizontal mirror plane through the Ti layer. In TiFBr, one F layer is

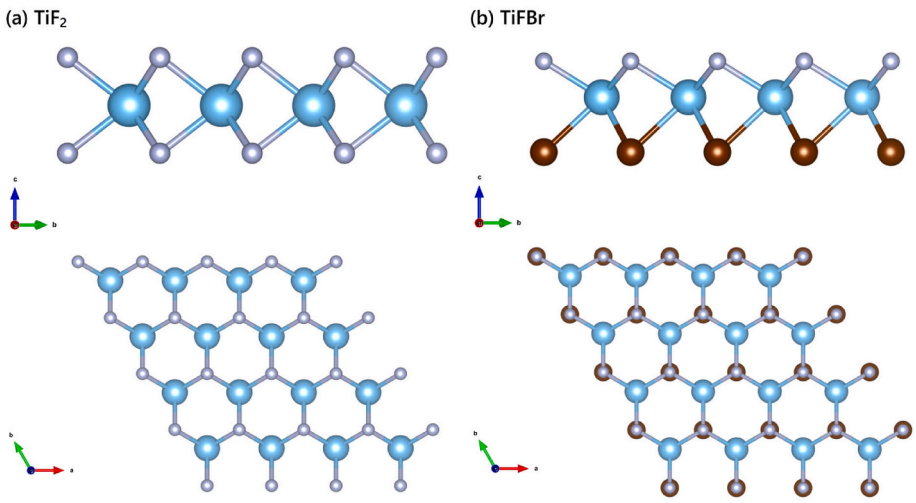


Fig. 1. Crystal structures of the 1H (a) TiF_2 and (b) Janus TiFBr monolayers, shown in side and top projection.

replaced by Br, making the two surfaces chemically distinct and removing this mirror plane; the symmetry is lowered to the polar space group P3m1 (No. 156, point group C_3v), which allows a net out-of-plane dipole. After relaxation the in-plane lattice parameter of TiFBr is 3.29 Å against 2.91 Å for TiF_2, an increase of 13.1%, and the Ti–Br bond (2.62 Å) is correspondingly longer than the Ti–F bonds (2.12 Å in TiF_2 and 2.24 Å in TiFBr); the relaxed structures are given in VASP POSCAR format in the Supplementary Material (Table S1). This follows from the covalent radius of bromine, 1.20 Å, exceeding that of fluorine, 0.57 Å [54]. For TiF_2, the 1H structure (denoted 2H in Ref. [26]) is also the lowest-energy monolayer polymorph: according to the PBE formation energies tabulated by Ono and Pawar [26], it lies 0.04 and 0.22 eV/atom below the distorted-octahedral 1T′ and octahedral 1T forms, respectively, and 0.12 eV/atom below fluorite-type bulk TiF_2.

The calculated elastic constants satisfy the Born–Huang criteria for a two-dimensional hexagonal lattice, $C_{11} > 0$, $C_{66} > 0$ and $C_{11} > |C_{12}|$, so both monolayers are mechanically stable against small in-plane strains [55]. For a hexagonal lattice C_{66} is not independent but equals $(C_{11} - C_{12})/2$, and the values in Table 2 obey this identity to within 0.01 N/m, which serves as an internal consistency check on the elastic calculation. The 2D Young's modulus is 96.05 N/m for TiF_2 and 73.61 N/m for TiFBr, so replacing one fluorine layer with bromine softens the sheet by roughly 23%, consistent with the longer and more polarisable Ti–Br bond. Both values are well below the 340 N/m of graphene but comparable to those reported for transition-metal dichalcogenide and Janus monolayers. The Poisson ratio is 0.21 for both monolayers. In two dimensions the shear modulus coincides with C_{66}, which is why these two columns of Table 2 carry identical values.

Phonon dispersion curves for TiF_2 and TiFBr (Fig. 2), obtained on a $4 \times 4 \times 1$ supercell using the finite-displacement method, show no imaginary branches across the Brillouin zone other than a small residual in the out-of-plane acoustic (ZA) branch near Γ. The residual reaches about −0.05 THz for TiF_2 and about −0.18 THz for TiFBr and is confined to wave vectors within 10–20% of the Γ–M distance, i.e., to wavelengths comparable to or longer than the $4 \times 4 \times 1$ supercell. This is the regime in which finite-displacement force constants are least accurate: the ZA branch of a two-dimensional crystal disperses quadratically, and small violations of the translational and rotational invariance conditions on a finite supercell produce spurious imaginary frequencies near Γ [56,57]. We therefore attribute the residual to this numerical artefact rather than to a structural instability, noting that a definitive confirmation would require force constants with the invariance conditions imposed or larger supercells. Both monolayers therefore most likely correspond to local minima on the potential-energy surface. The phonon spectrum reflects the atomic masses: in TiF_2 the light fluorine atoms dominate the high-frequency optical modes while titanium contributes mainly at low frequency, and in TiFBr the heavier bromine shifts part of this optical weight downward, compressing the overall phonon bandwidth relative to TiF_2.

Table 2
Calculated elastic constants C_{ij}, 2D Young's modulus E, and shear modulus G (all in N/m), together with the dimensionless Poisson ratio ν, for the TiF_2 and Janus TiFBr monolayers.

Monolayer	C_{11}	C_{12}	C_{66}	E	G	ν
TiF_2	100.69	21.61	39.54	96.05	39.54	0.21
TiFBr	77.06	16.29	30.38	73.61	30.38	0.21

In the MLFF-MD runs at 300 K (Figs. 3 and 4), the total energy fluctuates by about ±1 eV per 48-atom supercell (about ±0.02 eV/atom) without drift over 10 ps, and the temperature fluctuates around its target value of 300 K. Comparing the starting and final snapshots reveals neither broken bonds nor buckling or reconstruction of either surface; the mean Ti–F and Ti–Br bond lengths remain constant throughout the run, and the instantaneous lengths of individual bonds stay within 16.7% (Ti–F) and 13.1% (Ti–Br) of their mean values, as expected for thermal vibrations at 300 K (Fig. S1, Supplementary Material). TiF_2 and TiFBr monolayers are therefore mechanically and thermally stable, and most likely dynamically stable, in vacuum under near-ambient conditions; these tests do not address their chemical stability in water, which is discussed in Section 3.5.

3.2. Electronic Properties and Band-Edge Alignment

The HSE06 band structure of TiF_2 identifies it as an indirect-gap semiconductor with a band gap of 2.08 eV; the PBE calculation gives 1.24 eV. Janus TiFBr shows a direct band gap of 1.45 eV at the HSE06 level versus 0.98 eV at PBE (Fig. 5). Both HSE06 gaps exceed the 1.23 eV thermodynamic minimum for water splitting and fall below roughly 2.4 eV, the range usually quoted for single-absorber visible-light photocatalysis [58–60]. The 1.23 eV figure is a thermodynamic floor rather than a practical one: kinetic overpotentials at the two half-reactions add several tenths of an electronvolt (allowances of 0.2 eV for the HER and 0.6 eV for the OER are commonly assumed [31]), so a gap near 1.45 eV as found for TiFBr leaves little margin once these losses are included, whereas the 2.08 eV gap of TiF_2 provides a larger margin at the cost of a narrower absorption range; these margins are quantified in Section 3.4.

The PBE band structures and partial densities of states (PDOS) in Fig. S2 (Supplementary Material) show that the highest occupied band, which forms the valence-band maximum (VBM), is predominantly of Ti

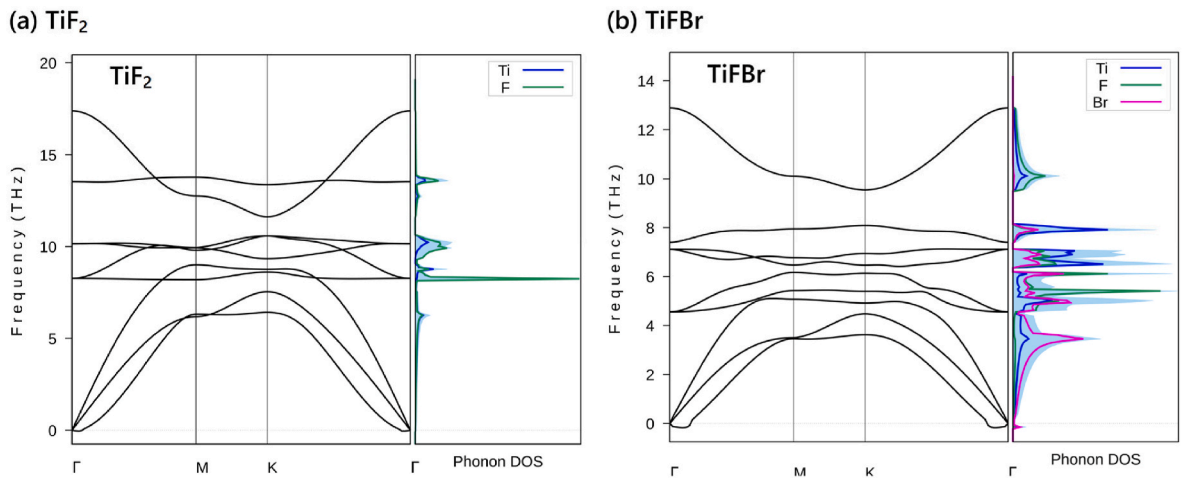


Fig. 2. Calculated phonon dispersions for (a) TiF_2 and (b) Janus TiFBr monolayers. The small imaginary ZA frequencies near Γ are discussed in the text.

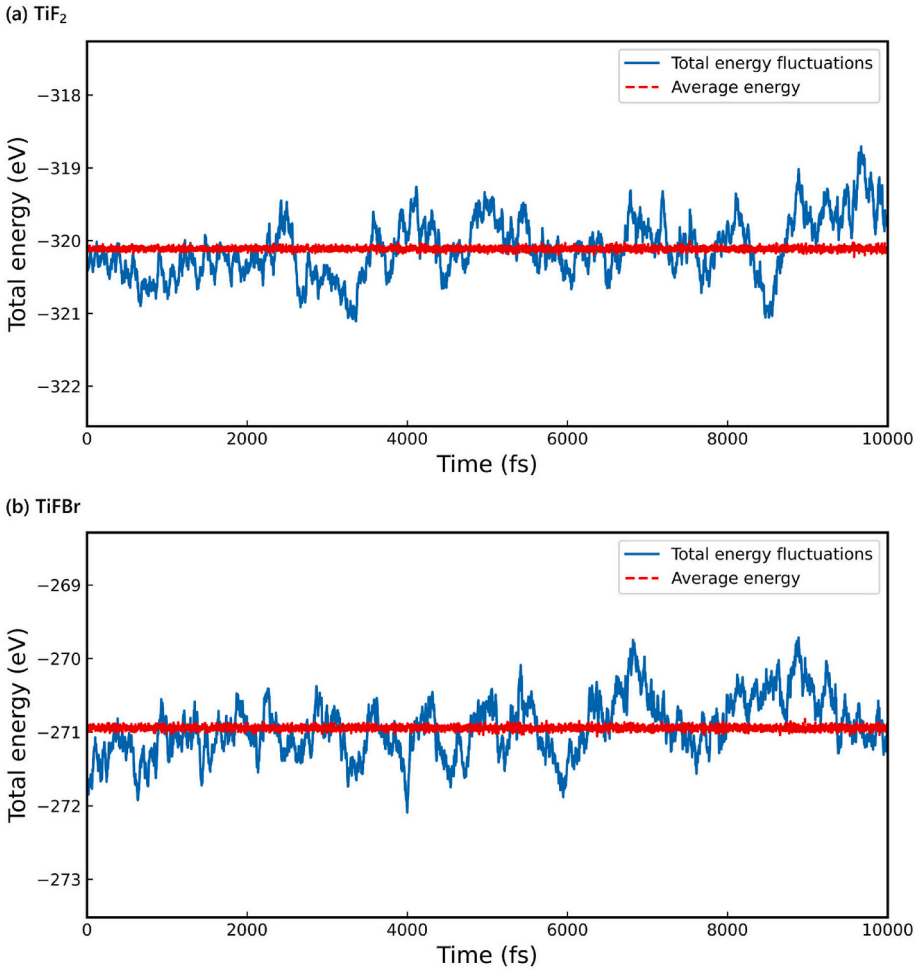


Fig. 3. Time evolution of the total energy over the MLFF-MD run at 300 K for (a) TiF_2 and (b) Janus TiFBr monolayers.

3d character, consistent with the formal d^2 configuration of Ti^{2+} and with other 1H d^2 systems [21]; the conduction-band minimum (CBM) is also of Ti 3d character. The halogen p bands lie much deeper: the highest Br 4p band of TiFBr lies about 2.3 eV below the VBM, and the F 2p bands of TiF_2 lie 5.46 eV below the VBM. These assignments follow from electron counting and the band topology of the 1H structure. The band gap is therefore of d–d type in both compounds. Relative to the vacuum level on the F-terminated side, the VBM of TiFBr lies 0.70 eV above that of TiF_2 (−5.29 versus −5.99 eV), whereas the CBM is almost unchanged (−3.84 versus −3.91 eV; see below), so the smaller gap of TiFBr stems mainly from its higher VBM. The work function is obtained from Ref. [61]:

$$\Phi = E_v^{ac} - E_F \quad \text{(Eq. 1)}$$

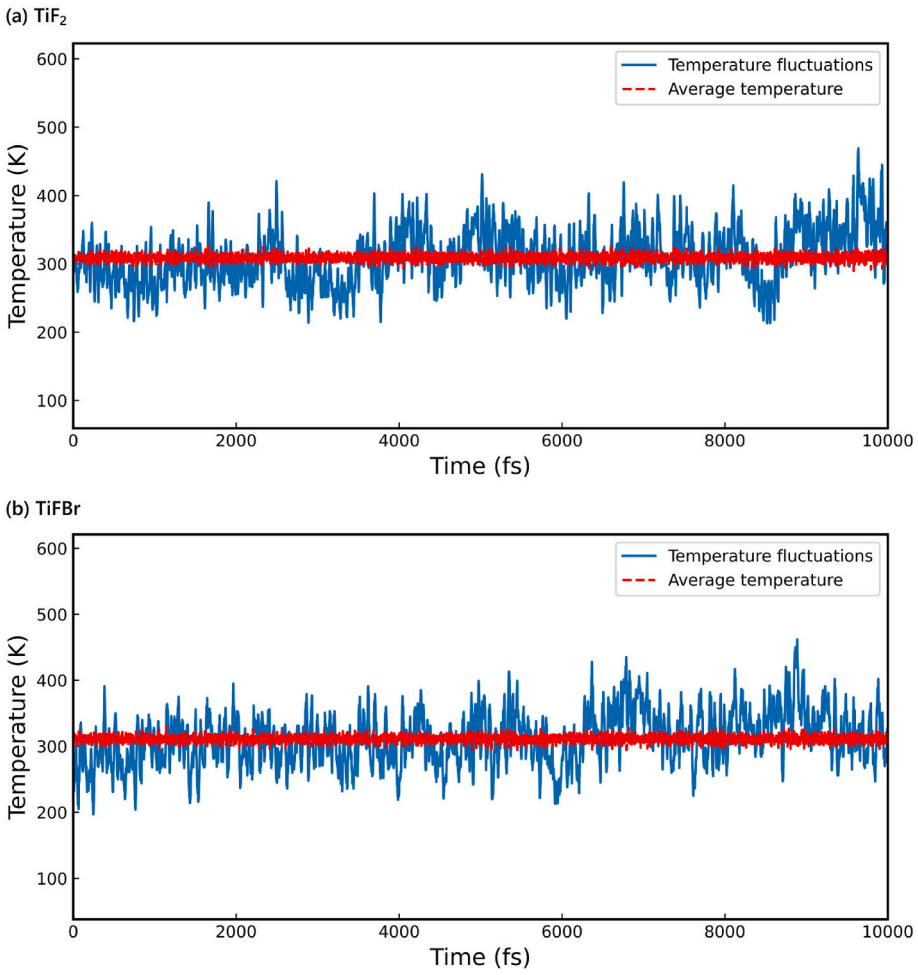


Fig. 4. Time evolution of the temperature over the MLFF-MD run at 300 K for (a) TiF_2 and (b) Janus TiFBr monolayers.

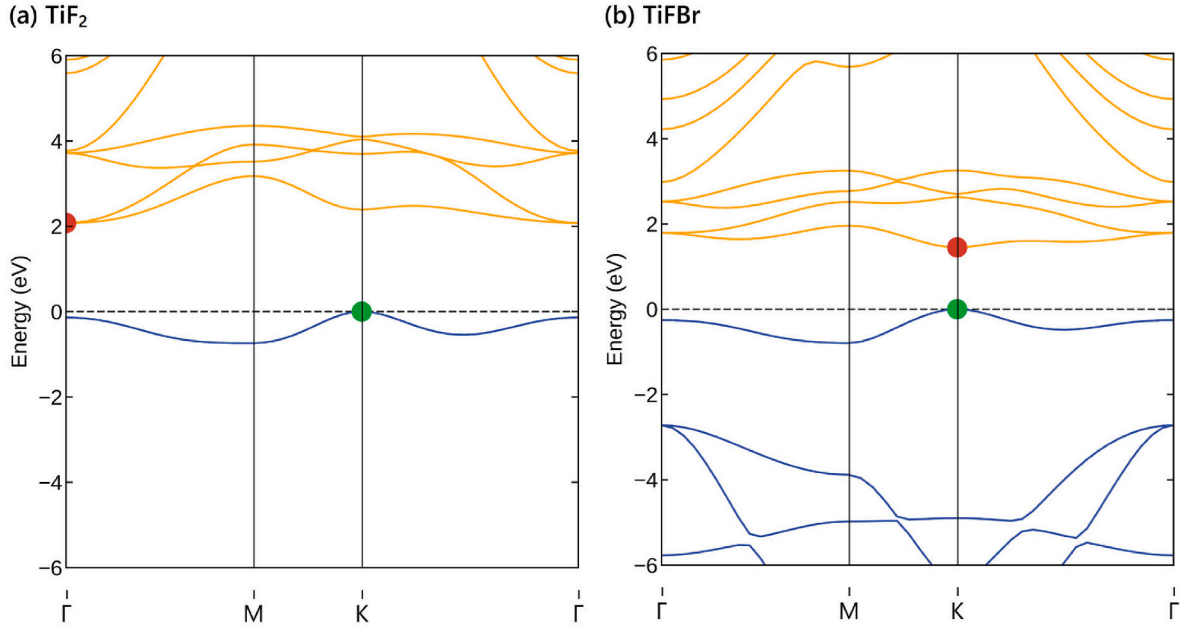


Fig. 5. HSE06 electronic band structures of (a) TiF_2 and (b) Janus TiFBr monolayers.

where E_v^{ac} is the potential energy of an electron in the vacuum region, taken from the planar-averaged electrostatic potential (Fig. 6), and E_F the Fermi level. For the mirror-symmetric TiF_2 monolayer a single value

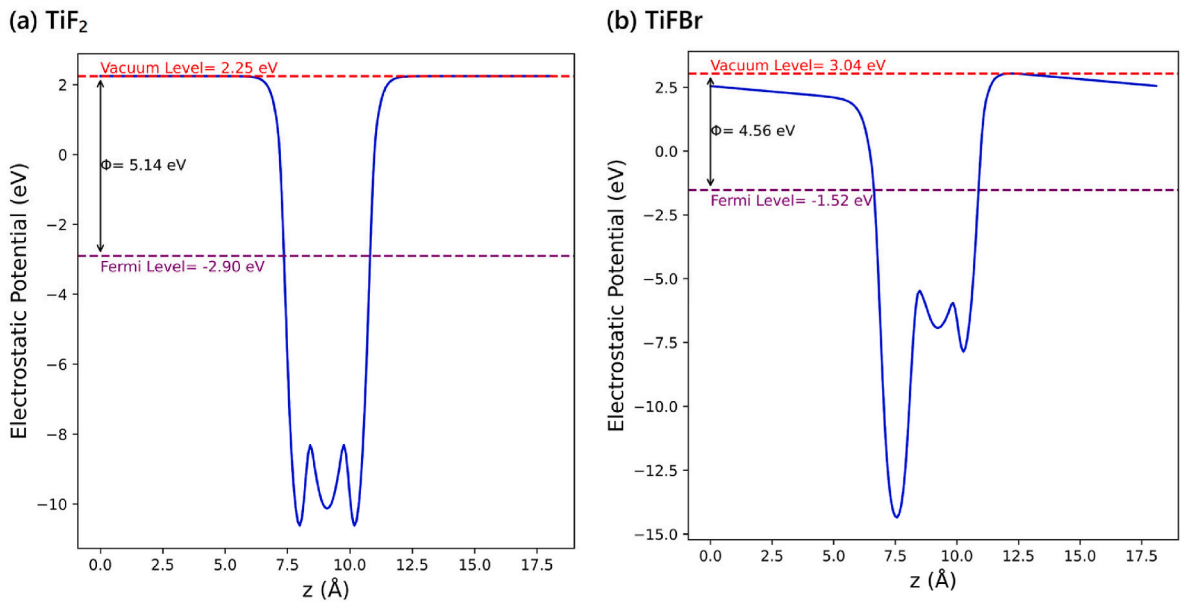


Fig. 6. Planar-averaged electrostatic potential along the surface normal for the (a) TiF_2 and (b) Janus TiFBr monolayers. The vacuum level (red) and Fermi level (purple) are marked, and the arrow indicates the work function Φ (of the F-terminated face for TiFBr). The two vacuum levels are equivalent for TiF_2. For TiFBr, the linear slope of the potential in the vacuum region (about 0.085 V $Å^{-1}$) is the compensating field of the periodic cell (no dipole correction), so the two ends of the curve, which correspond to the same point of the periodic cell, have the same value. The red line marks the potential just outside the F-terminated face (3.04 eV), which is used as the reference; it exceeds the potential just outside the Br-terminated face (about 2.09 eV) by about 0.95 eV, and the dipole-corrected vacuum-level difference is estimated to lie roughly between 0.95 and 1.55 eV (Section 3.2).

of 5.14 eV applies to both surfaces. For Janus TiFBr the loss of mirror symmetry makes the two vacuum levels inequivalent, so the work function is face-dependent; the value of 4.56 eV reported here refers to the fluorine-terminated side and, since no dipole correction was applied, is an estimate that depends on the chosen reference point (see below); the Br-terminated side has a lower work function (Fig. 6(b)).

The electrostatic potential profiles in Fig. 6 show the origin of this difference. For TiF_2 the potential converges to the same vacuum level of 2.25 eV on both sides of the slab, as required by its mirror symmetry, and the Fermi level sits at −2.90 eV. For TiFBr the potential in the vacuum region is not flat but decreases linearly from the F-terminated face, across the cell boundary ($z = 0 \equiv 18.17$ Å), to the Br-terminated face, with a slope of about 0.085 V $Å^{-1}$ (Fig. 6(b)). This slope is the artificial compensating field that arises when a polar slab is treated in a periodic cell without a dipole correction [62,63]. As a result, the potential just outside the fluorine-terminated face (3.04 eV) exceeds that just outside the bromine-terminated face (about 2.09 eV) by about 0.95 eV, whereas the two ends of the curve, which correspond to the same point of the periodic cell, have the same value.

Because no self-consistent dipole correction was applied, the face-dependent vacuum levels of TiFBr can only be estimated, and the following numbers indicate the likely scale of the effect rather than validated bounds. Over one cell height the compensating field changes the potential by 0.085 V $Å^{-1}$ × 18.17 Å ≈ 1.55 eV, part of which falls inside the slab; the dipole-corrected vacuum-level difference ΔΦ is therefore expected to lie roughly between these two values, $0.95\ \text{eV} \lesssim \Delta\Phi \lesssim 1.55\ \text{eV}$. This offset is the electrostatic signature of the intrinsic out-of-plane dipole. Because the potential energy of an electron in the vacuum is higher on the F-terminated side (i.e., the electrostatic potential is lower there), the built-in field is directed from the bromine-terminated toward the fluorine-terminated face; it drives photo-generated electrons toward the Br-terminated face, where the conduction band lies higher relative to the local vacuum level, and holes toward the F-terminated face, where the valence band lies deeper [30]. The band edges and work function of TiFBr quoted here are referenced to the potential just outside the F-terminated face (3.04 eV). Because the compensating field also acts over the ≈3 Å between the middle of the slab and this reference point, the band edges (and the Fermi level) obtained in this way are probably too high: allowing for partial screening inside the slab, we estimate that dipole-corrected band edges might lie roughly 0.1–0.25 eV deeper (0.085 V $Å^{-1}$ × ≈3 Å ≈ 0.25 eV without screening), and the F-side work function would be larger by the same amount (still below the 5.14 eV of TiF_2). This would shift the TiFBr window limits derived below to lower pH by about 2–4 units (0.1–0.25 eV divided by 0.059 eV per pH unit).

In TiF_2 the valence and conduction edges fall at −5.99 eV and −3.91 eV; the equivalent edges in TiFBr sit at −5.29 eV and −3.84 eV. Their HSE06 alignment is sketched for both monolayers in Fig. 7. TiF_2 satisfies both criteria at pH = 0, with a band-edge offset of 0.32 eV for the OER and 0.53 eV for the HER; the HER driving force shrinks as pH rises and vanishes at pH 9.0, which sets the upper limit of its window. TiFBr does not meet the VBM requirement at pH = 0, where its valence edge lies 0.38 eV above the oxygen evolution level. At pH = 7 the oxidation level has shifted to −5.26 eV and the TiFBr valence edge at −5.29 eV lies only 0.03 eV below it, so the driving force for oxygen evolution at neutral pH is small; it grows to 0.21 eV at pH 10, close to the upper bound of the window set by the HER condition.

The pH-dependent positions of the water redox potentials follow [64]:

$$E^{H^+}/{}^{H_2}(\text{pH}) = -4.44 + 0.059 \times \text{pH eV} \quad \text{(Eq. 2)}$$

$$E_{o2}/{}^{H_{2o}}(\text{pH}) = -5.67 + 0.059 \times \text{pH eV} \quad \text{(Eq. 3)}$$

Comparing these Nernst-shifted levels with the calculated band edges defines the operating window of each monolayer. For TiF_2 the OER condition E_VBM < E_O_2/H_2O is met at every pH: the valence edge at −5.99 eV already lies below the oxygen evolution level at pH 0, and that level rises with pH, reaching −4.84 eV at pH 14. The limiting requirement is therefore the HER condition E_CBM > E_H^+/H_2, which gives $-3.91 > -4.44 + 0.059$ pH and holds up to pH 9.0. TiF_2 thus straddles both potentials from pH 0 to about pH 9.0. For TiFBr the roles are reversed. Its shallower valence edge at −5.29 eV satisfies the OER condition only above pH 6.4, while its conduction edge at −3.84 eV meets the HER condition up to pH 10.2, so the active window runs from

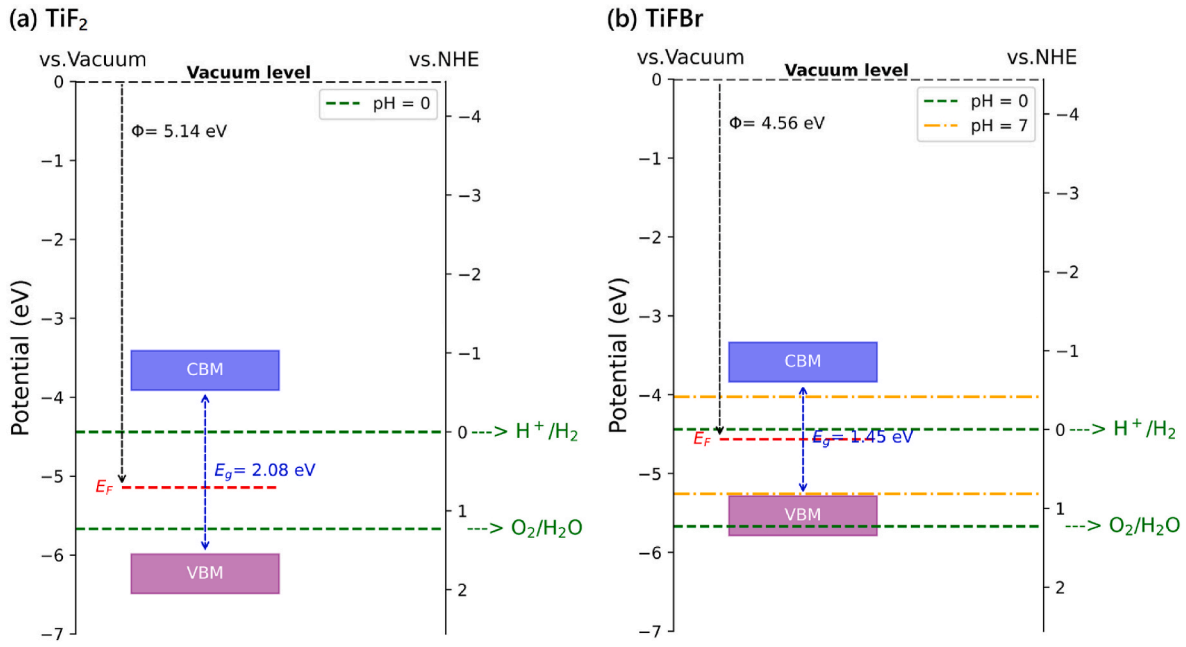


Fig. 7. HSE06 band-edge positions of the (a) TiF_2 and (b) Janus TiFBr monolayers on the vacuum and NHE scales, with the work function Φ and the Fermi level E_F indicated (TiFBr: referenced to the vacuum level on the F-terminated side). The water reduction and oxidation potentials are shown at pH = 0 for both panels and additionally at pH = 7 for TiFBr.

roughly pH 6.4 to pH 10.2 (Fig. 8; F-side reference, see below). TiF_2 therefore satisfies the thermodynamic criteria in the acidic and near-neutral range and TiFBr from neutral to alkaline conditions, and the two overlap between pH 6.4 and 9.0, where either monolayer satisfies both half-reactions. Together the two windows span pH 0–10.2 rather than the full pH scale, and these thermodynamic windows narrow considerably once kinetic overpotentials are taken into account (Section 3.4). These windows are screening estimates: the vacuum-referenced band edges are held fixed while the redox levels shift with pH (Eqs. (2) and (3)), and electrolyte-induced band-edge shifts and surface chemistry are not included. For the Janus layer, the analysis above references both band edges to the F-side vacuum level; the estimated dipole correction would move the TiFBr window by 2–4 pH units toward acidic conditions. Relative to the vacuum level on the Br-terminated side, which is lower by ΔΦ, the CBM lies at −3.84 eV + ΔΦ, i.e., at about −2.9 eV (for ΔΦ = 0.95 eV) or higher. If the HER takes place on the Br-terminated face, toward which the built-in field drives the electrons, the HER condition is therefore met at all pH, and the window of TiFBr is limited only by the OER condition on the F-terminated face (pH $\gtrsim$ 6.4) [30,31]. This is a thermodynamic argument based on the band edges and the electrostatic potential; the reaction intermediates were not computed (Section 3.5). The internal electric field can thus promote

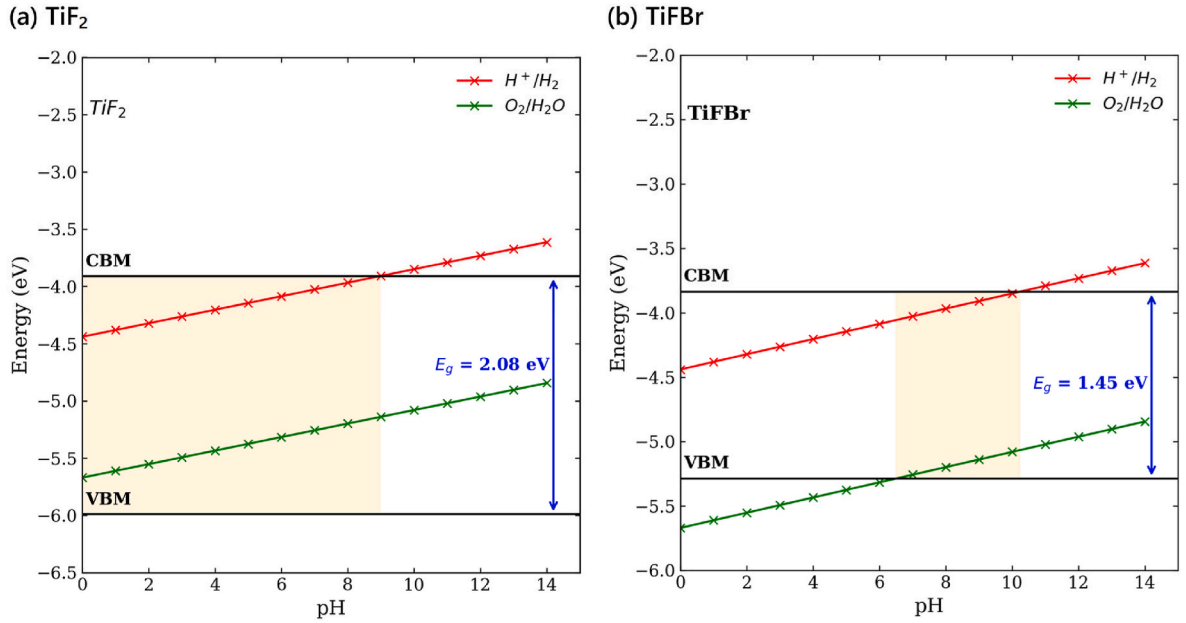


Fig. 8. HSE06 band edges of the (a) TiF_2 and (b) Janus TiFBr monolayers compared with the water reduction and oxidation potentials as a function of pH. The pH range over which both redox conditions are satisfied is highlighted with a yellow rectangle. TiFBr band edges are referenced to the vacuum level on the F-terminated side.

the spatial separation of photogenerated carriers [28,61]; because both band edges are of Ti 3d character, however, this separation is expected to be partial, and quantifying it would require an analysis of the band-decomposed charge densities.

3.3. Optical Properties

Optical response is reported as absorptance, reflectance, and transmittance, which are dimensionless fractions rather than the bulk absorption coefficient α(ω). They were obtained for a free-standing layer at normal incidence from the sheet conductivity $\sigma_{2D}(\omega) = i\varepsilon_0\omega L[1 - \varepsilon(\omega)]$, where ε(ω) is the in-plane dielectric function computed for the supercell of height L [48,49]:

$$A(\omega) = \mathrm{Re}\,\tilde{\sigma}(\omega) \;/\; |1 + \tilde{\sigma}(\omega)/2|^2 \qquad \text{(Eq. 4)}$$

$$R(\omega) = |\tilde{\sigma}(\omega)/2|^2 \;/\; |1 + \tilde{\sigma}(\omega)/2|^2 \qquad \text{(Eq. 5)}$$

$$T(\omega) = 1 \;/\; |1 + \tilde{\sigma}(\omega)/2|^2 \qquad \text{(Eq. 6)}$$

where $\tilde{o} = \sigma_{2D}/(\varepsilon_0 c)$. Because ε(ω) − 1 scales as 1/L, σ_{2D} and hence A, R and T are independent of the vacuum thickness, and no effective layer thickness is needed; they represent the fraction of incident light absorbed, reflected or transmitted by a single free-standing layer. At each photon energy the three quantities satisfy A + R + T = 1 by energy conservation; the values quoted below are rounded independently, so their sums may deviate from unity by up to 0.1 percentage points. The dielectric functions in Fig. 9(a) and 10(a), by contrast, are those of the supercell (L ≈ 18 Å), so their absolute magnitudes depend on L. The spectra in Figs. 9 and 10 were computed at the PBE level in the independent-particle approximation (Table 1). Since PBE underestimates the gap, the interband transitions in these figures appear at too low energies, which is why the absorption maxima lie below the HSE06 gaps; within the scissor approximation they are shifted rigidly by the HSE06–PBE gap difference. The scissor-corrected spectra, obtained by shifting $\varepsilon_2(\omega)$ rigidly by Δ = 0.84 eV for TiF_2 and 0.47 eV for TiFBr, are summarised in Table 3 and Fig. 11. For these spectra, Re $\tilde{o} = (\omega L/c)\varepsilon_2$ was obtained from the computed PBE absorptance by inverting Eq. (4), shifted rigidly and inserted again into Eq. (4); the term $(\mathrm{Im}\,\tilde{o}/2)^2$, which involves ε_1, contributes less than about 0.5% to the denominator of Eq. (4) for these monolayers and was neglected, so that no Kramers–Kronig transformation of the shifted spectra was required. AM1.5G-weighted quantities were integrated over 0.31–4.43 eV (280–4000 nm), within the computed spectral range. Unless stated otherwise, energies quoted in the remainder of this section refer to the PBE spectra.

Fig. 9(a) and 10(a) present the real and imaginary parts of the complex dielectric function, $\varepsilon_1(\omega)$ and $\varepsilon_2(\omega)$, along the xx and yy directions for TiF_2 and TiFBr, respectively. The static value $\varepsilon_1(0)$ is approximately 4.9 for TiF_2 and 7.0 for TiFBr (supercell values for cells of nearly equal height); the larger value for the Janus monolayer is consistent with its smaller band gap through the Penn relation, since $\varepsilon_1(0) - 1$ scales inversely with the square of an effective gap. The principal maximum of $\varepsilon_1(\omega)$ occurs at 1.3 eV for TiF_2 and 0.95 eV for TiFBr, in both cases just below the main ε_2 peak, as expected from the Kramers–Kronig relation between the real and imaginary parts. Above

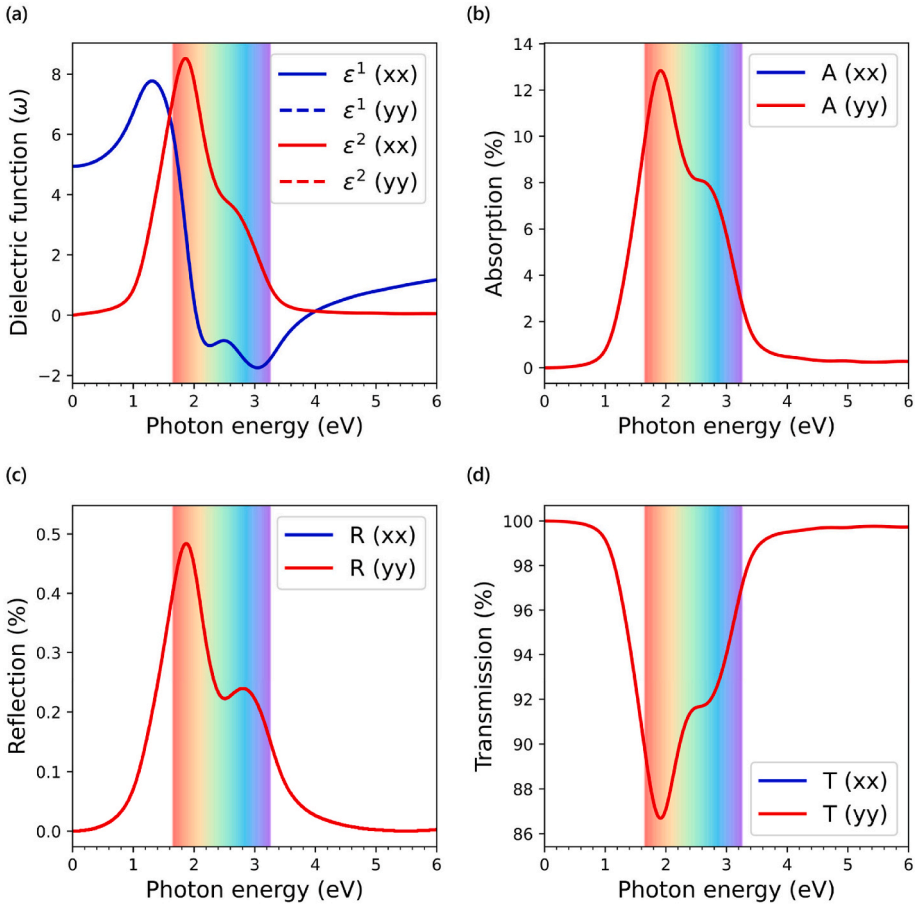


Fig. 9. Optical response of the TiF_2 monolayer between 0 and 6 eV calculated at the PBE level: (a) supercell dielectric function split into its real $\varepsilon_1(\omega)$ and imaginary $\varepsilon_2(\omega)$ parts, together with (b) absorptance, (c) reflectance and (d) transmittance. A rainbow bar delimits the visible window; xx and yy components are indistinguishable. Scissor-corrected spectra are shown in Fig. 11.

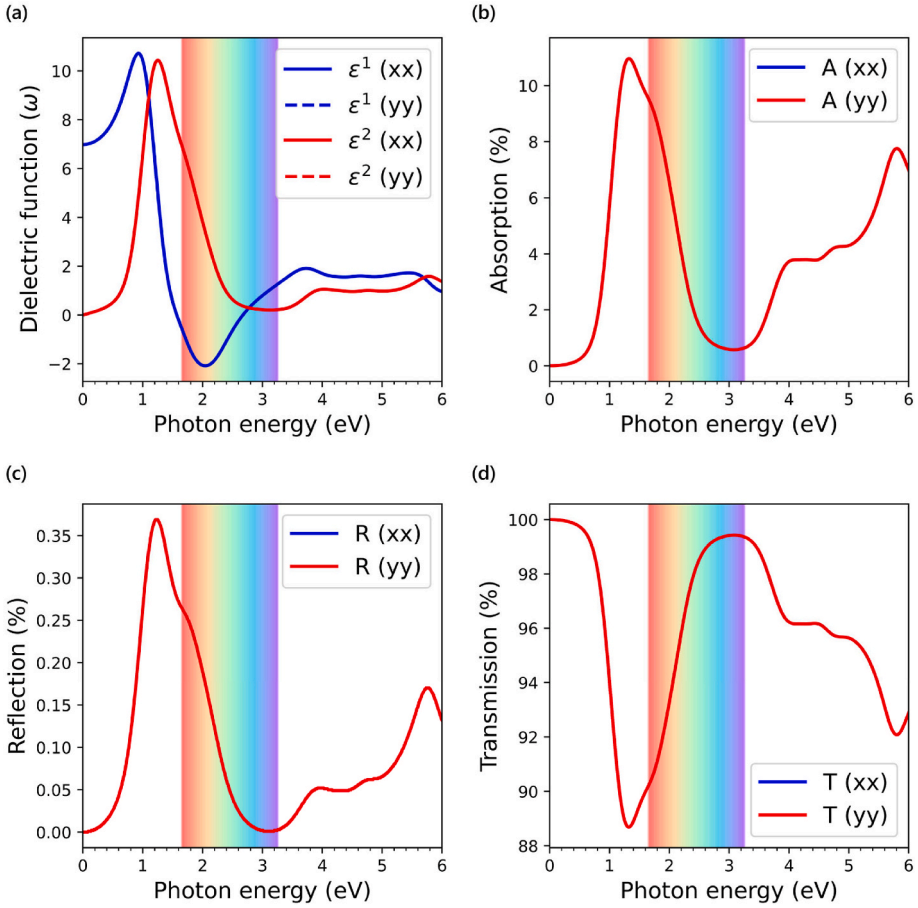


Fig. 10. Optical response of the Janus TiFBr monolayer between 0 and 6 eV calculated at the PBE level: (a) supercell dielectric function split into its real $\varepsilon_1(\omega)$ and imaginary $\varepsilon_2(\omega)$ parts, together with (b) absorptance, (c) reflectance and (d) transmittance. A rainbow bar delimits the visible window; xx and yy components are indistinguishable. Scissor-corrected spectra are shown in Fig. 11.

Table 3
Main absorption peak of the TiF_2 and Janus TiFBr monolayers from the PBE spectra and after the scissor correction ($\Delta = E_g^{HSE06} - E_g^{PBE}$), together with the AM1.5G photon flux absorbed by a single layer (absorptance set to zero below the HSE06 gap), expressed as an equivalent current density J_{abs}, and the corresponding value for complete absorption above the HSE06 gap, J_{max}. Peak positions are given to ±0.05 eV.

Monolayer	Δ (eV)	PBE peak: E (eV)/A (%)	Corrected peak: E (eV)/λ (nm)/A (%)	J_{abs} (mA cm^{-2})	J_{max} (mA cm^{-2})
TiF_2	0.84	1.95/12.9	≈2.8/≈445/17	1.5	12.9
TiFBr	0.47	1.35/11.0	≈1.8/≈690/14	3.1	30.8

these maxima $\varepsilon_1(\omega)$ falls steeply and becomes negative, reaching −1.8 near 3.1 eV for TiF_2 and −2.1 near 2.1 eV for TiFBr. A negative ε_1 does not imply metallic character, which is excluded here by the finite band gap; it marks a spectral region of anomalous dispersion immediately above a strong interband transition. Both curves recover positive values by 4 eV. The xx and yy components coincide throughout, consistent with the in-plane isotropy imposed by the threefold rotational symmetry of both point groups (D_3h and C_3v).

Fig. 9(b) and 10(b) show the in-plane absorptance obtained at the PBE level. TiF_2 rises sharply from an onset near 1.2 eV to a maximum of 12.9% at 1.95 eV, with a shoulder at 2.6 eV, before decaying above 3.3 eV. TiFBr reaches a lower maximum (11.0%) at lower energy (1.35 eV); its absorptance then falls to a minimum of about 0.6% between 2.8 and 3.2 eV before a second interband feature grows above 4 eV and reaches 7.7% at 5.8 eV. After the scissor correction (Table 3 and Fig. 11), the main absorption peak of TiF_2 moves to about 2.8 eV (about 445 nm, blue) and that of TiFBr to about 1.8 eV (about 690 nm, red), and the peak absorptances rise to about 17% and 14%, respectively. The increase arises because, for a weakly absorbing sheet, Eq. (4) reduces to $A(\omega) \approx \mathrm{Re}\,\tilde{o}(\omega) = (\omega L/c)\,\varepsilon_2(\omega)$, i.e., A is proportional to the product of the photon energy and ε_2; a rigid shift of ε_2 by Δ therefore multiplies the absorptance by roughly $\hbar\omega/(\hbar\omega - \Delta)$, which raises the main peaks by about 30–40%. The corrected spectra therefore place the leading transitions of both monolayers inside the visible range, with TiFBr absorbing most strongly in the red and TiF_2 in the blue, although the two bands overlap between about 2.1 and 2.6 eV; the absorption minimum of TiFBr moves to about 3.3–3.7 eV.

Weighting the corrected spectra with the AM1.5G photon flux [53], with the absorptance set to zero below the HSE06 gap to remove the broadening tail, gives absorbed photon fluxes equivalent to 1.5 mA cm^{-2} for TiF_2 and 3.1 mA cm^{-2} for TiFBr, about 12% and 10% of the photons available above the respective gaps (12.9 and 30.8 mA cm^{-2}). A single TiFBr layer thus absorbs about twice as many solar photons as a TiF_2 layer, because its absorption band lies at lower photon energies, where the AM1.5G photon flux is larger. Absorptance values of 10–20% for a single layer are typical for 2D semiconductors and correspond to strong absorption per unit thickness [65], but a single layer captures only a small fraction of the incident sunlight: for N electronically decoupled layers, neglecting reflection and interference, $J_{abs,N} = q\int\Phi(E)\,[1 - (1 - A_1(E))^N]\,dE$ gives about 69% (TiF_2) and 62% (TiFBr) of the above-gap photons for N = 10. Practical devices would therefore rely on multilayer stacking or light trapping, or on heterostructures [66].

The reflectance spectra in Fig. 9(c) and 10(c) track the absorptance

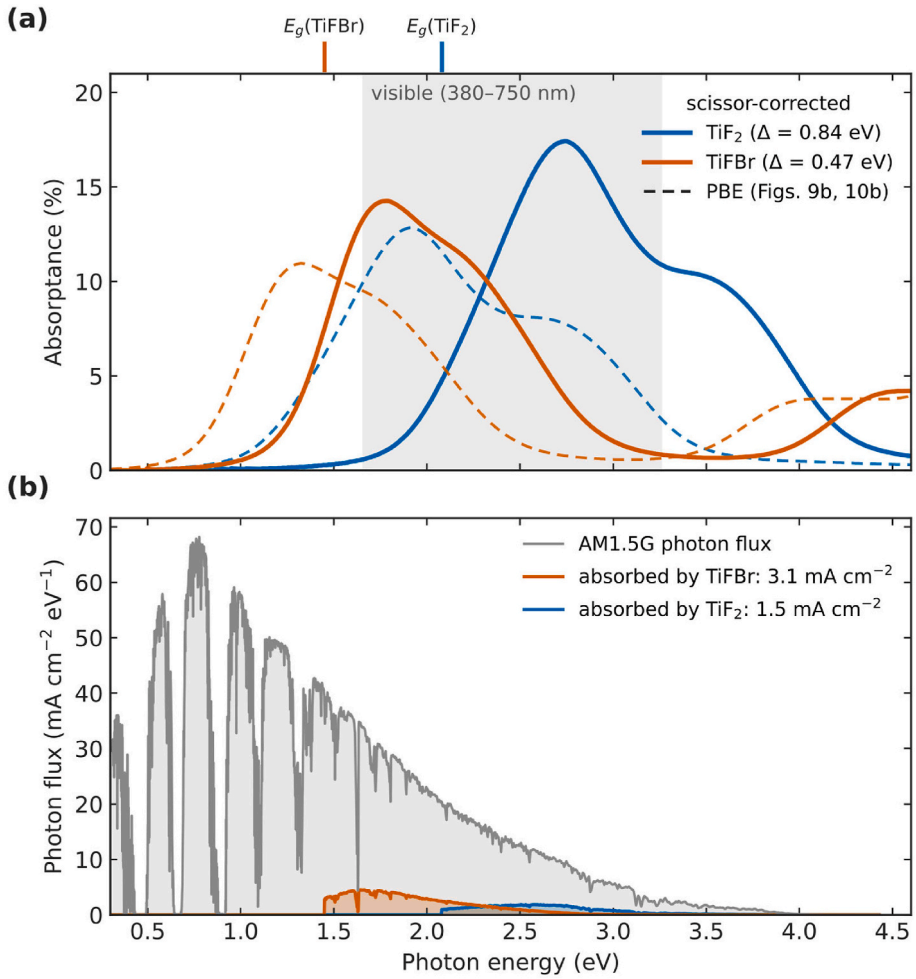


Fig. 11. (a) Scissor-corrected absorptance of the TiF_2 (blue) and Janus TiFBr (orange) monolayers (solid lines) compared with the PBE spectra of Fig. 9(b) and 10(b) (dashed lines); the ticks above the panel mark the HSE06 gaps and the grey band the visible range. (b) AM1.5G photon flux and the photon flux absorbed by a single layer of each monolayer (absorptance set to zero below the HSE06 gap), expressed as equivalent current densities.

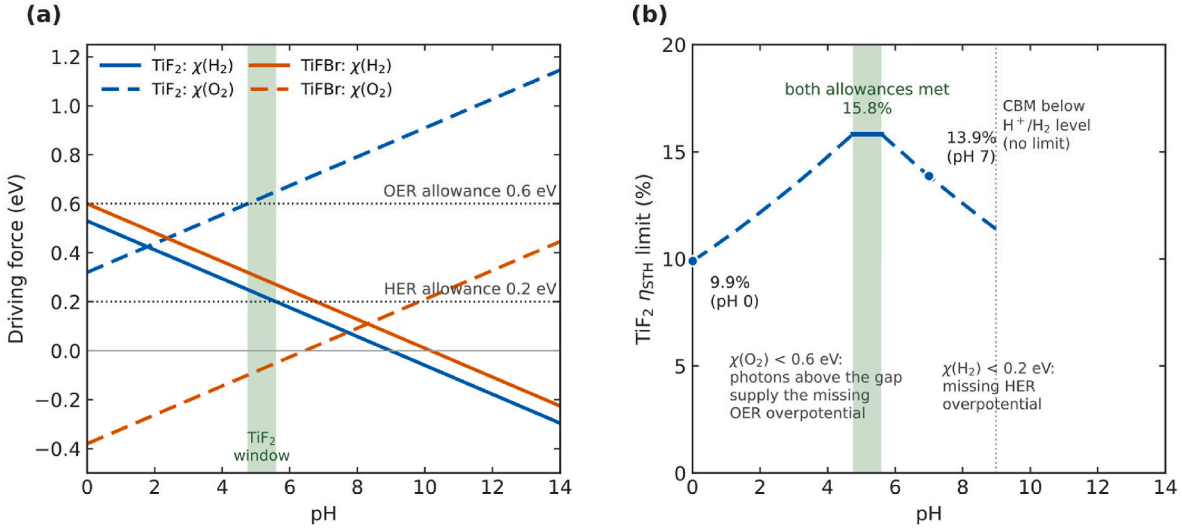


Fig. 12. (a) Driving forces $\chi(H_2)$ (solid lines) and $\chi(O_2)$ (dashed lines) of TiF_2 (blue) and TiFBr (orange; F-side reference) as a function of pH, compared with the overpotential allowances of 0.2 eV (HER) and 0.6 eV (OER) (dotted lines); the green band marks the window in which TiF_2 meets both allowances. (b) Theoretical STH efficiency limit of TiF_2 from Eqs. (7)–(9), assuming that all photons above the gap are absorbed. Between pH 4.7 and 5.6 (solid line, green band) the band edges provide both allowances and the limit is 15.8%; outside this range (dashed line) part of the photon energy must supply the missing overpotential, which lowers the limit (9.9% at pH 0 and 13.9% at pH 7; idealised upper bounds of the model); above pH 9.0 the conduction band lies below the H^+/H_2 level and no limit is defined. No limit is shown for TiFBr (see text).

curves, as expected when both derive from the same interband transitions. Reflectance vanishes at zero photon energy and peaks at 0.48% at 1.87 eV for TiF_2 and at 0.37% at 1.25 eV for TiFBr. These values are below one percent throughout, so reflection losses are negligible for a free-standing monolayer and essentially all light that is not absorbed is transmitted.

Fig. 9(d) and 10(d) show the corresponding transmittance. TiF_2 falls to a minimum of 86.7% at 1.95 eV, mirroring its absorptance maximum, and recovers to above 99% beyond 4 eV. TiFBr reaches its minimum of 88.7% at 1.35 eV, then rises to a maximum of 99.4% near 3.1 eV, where in the PBE spectrum the material is almost transparent across the blue and violet range, and decreases steadily thereafter to 92% at 6 eV as the ultraviolet interband transitions switch on. The monotonic ultraviolet decrease for TiFBr is the complement of the second absorptance feature noted above.

3.4. Driving Forces, Operating Windows and Solar-To-Hydrogen Efficiency

The band-edge criteria used in Section 3.2 are thermodynamic. To drive the reactions at useful rates, photogenerated carriers must also overcome kinetic overpotentials, for which allowances of 0.2 eV for the HER and 0.6 eV for the OER are commonly adopted when 2D photocatalysts are assessed [31,52]. Fig. 12(a) compares the driving forces $\chi(H_2) = E_{CBM} - E^{+}_{H2}$ and $\chi(O_2) = E_{O2/H2O} - E_{VBM}$ with these allowances, and Table 4 summarises the resulting windows. For TiF_2, $\chi(H_2)$ decreases from 0.53 eV at pH 0 while $\chi(O_2)$ increases from 0.32 eV, so both allowances are met only between pH 4.7 and 5.6; the thermodynamic window of pH 0–9.0 thus contracts to a narrow, mildly acidic range once kinetic losses are included. Because the gap of TiF_2 exceeds 1.23 eV + 0.8 eV by only 0.05 eV, this window is sensitive to the uncertainty of the computed band edges. For TiFBr with a common F-side vacuum reference, the two driving forces add up to $\chi(H_2) + \chi(O_2) = E_g - 1.23$ eV = 1.45 − 1.23 = 0.22 eV at every pH; this total is well below the 0.2 + 0.6 = 0.8 eV required by the two allowances, so they cannot be met simultaneously at any pH. Within the thermodynamic window (pH 6.4–10.2), $\chi(O_2) = -0.38$ eV + 0.059 eV × pH rises from zero at pH 6.4 to only 0.22 eV at pH 10.2. The built-in field of TiFBr raises the conduction band on the Br-terminated face (Section 3.2) but does not deepen the valence band relative to the F-side vacuum level: in a two-face model in which hydrogen evolves on the Br-terminated face, the OER allowance on the F-terminated face would still require pH ≈ 16.6, outside the 0–14 range (≈12.4 if the dipole-corrected band edges lie 0.25 eV deeper). Within these models, TiFBr is therefore not expected to sustain overall water splitting on its own, although its conduction band offers a large driving force for hydrogen evolution, for example in the presence of a sacrificial electron donor.

Table 4
Driving forces for the HER and OER at pH 0 and 7, thermodynamic operating windows, windows with overpotential allowances of 0.2 eV (HER) and 0.6 eV (OER), and theoretical STH efficiency limits. TiFBr band edges are referenced to the vacuum level on the F-terminated side.

System	$\chi(H_2)$, pH 0/7 (eV)	$\chi(O_2)$, pH 0/7 (eV)	Thermodynamic window (pH)	Window with allowances (pH)	η_{STH} limit (%)
TiF_2	0.53/ 0.12	0.32/ 0.73	0–9.0	4.7–5.6	15.8 (pH 4.7–5.6); 9.9 (pH 0)[a]; 13.9 (pH 7)[a]
TiFBr	0.60/ 0.19	−0.38/ 0.03	6.4–10.2[b]	none[c]	–[c]

[a] Outside the window, Eqs. (7)–(9) assume that photons above the gap supply the missing overpotential (idealised upper bound).

[b] TiFBr edges referenced to the F-side vacuum level; dipole-corrected edges might lie roughly 0.1–0.25 eV deeper (Section 3.2), which would shift these limits to lower pH by about 2–4 units.

[c] $\chi(H_2) + \chi(O_2) = E_g - 1.23$ eV = 0.22 eV < 0.8 eV, so the two allowances cannot be met simultaneously; even in a two-face model with hydrogen evolution on the Br-terminated face, the OER allowance would require pH ≈ 16.6 (≈12.4 for band edges 0.25 eV deeper). In the branch where both driving forces fall below their allowances (pH ≳ 6.8 within the thermodynamic window), Eqs. (7)–(9) with a common reference formally return about 17%, which is the value for an ideal 2.03 eV absorber for any material ($E = E_g + 0.8$ eV − $\chi(H_2) - \chi(O_2) = 2.03$ eV) and is therefore not a property of TiFBr.

The theoretical STH efficiency limit is the product of the light-absorption efficiency η_{abs} and the carrier-utilisation efficiency η_{cu} [31]:

$$\eta_{abs} = \int_{Eg}^{\infty} P(\hbar\omega)\, d(\hbar\omega) \Big/ \int_{0}^{\infty} P(\hbar\omega)\, d(\hbar\omega) \quad \text{(Eq. 7)}$$

$$\eta_{cu} = \Delta G \int_{E}^{\infty} [P(\hbar\omega) / \hbar\omega] d(\hbar\omega) \Big/ \int_{Eg}^{\infty} P(\hbar\omega)\, d(\hbar\omega) \quad \text{(Eq. 8)}$$

$$\eta_{STH} = \eta_{abs} \times \eta_{cu} \quad \text{(Eq. 9)}$$

where $P(\hbar\omega)$ is the AM1.5G spectral irradiance [53], $\Delta G = 1.23$ eV, and E is the lowest photon energy that can be used once the allowances are imposed: $E = E_g$ if $\chi(H_2) \geq 0.2$ eV and $\chi(O_2) \geq 0.6$ eV; $E = E_g + 0.2$ eV − $\chi(H_2)$ if $\chi(H_2) < 0.2$ eV and $\chi(O_2) \geq 0.6$ eV; $E = E_g + 0.6$ eV − $\chi(O_2)$ if $\chi(H_2) \geq 0.2$ eV and $\chi(O_2) < 0.6$ eV; and $E = E_g + 0.8$ eV − $\chi(H_2) - \chi(O_2)$ otherwise [31].

The results are shown in Fig. 12(b) and Table 4. For TiF_2 (E_g = 2.08 eV), 33.1% of the AM1.5G power lies above the gap (η_{abs} = 33.1%). Between pH 4.7 and 5.6 both allowances are met, so that $E = E_g$, η_{cu} = 47.8% and η_{STH} = 15.8%. Outside this range, part of the photon energy must supply the missing overpotential, which raises E and lowers the limit: at pH 0, $\chi(O_2) = 0.32$ eV, so that $E = E_g + 0.6$ eV − 0.32 eV = 2.36 eV, η_{cu} = 29.9% and η_{STH} = 9.9%; at pH 7, $\chi(H_2) = 0.12$ eV, so that E = 2.16 eV and η_{STH} = 13.9%. These values are idealised upper bounds of the adopted model rather than predicted efficiencies; outside the window they additionally assume that the excess photon energy can supply the missing overpotential, which is not guaranteed once carriers have relaxed to the band edges. These limits assume that every photon above the indirect gap is absorbed; taking the lowest direct transition, about 0.1 eV higher, as the absorption threshold lowers the limit to about 13%, and with the computed absorptance of a single layer (Section 3.3) the limit inside the window is about 1.9%. For TiFBr, the band edges do not provide both allowances at any pH below ≈12, so no meaningful STH limit can be given (Table 4, footnote c).

3.5. Chemical Stability, Synthesis and Scope of the Present Assessment

The tests in Section 3.1 indicate that both monolayers are most likely local minima of the potential-energy surface that withstand thermal agitation in vacuum; they do not establish thermodynamic stability with respect to competing phases, nor chemical stability in water. For TiF_2, the 1H monolayer is the lowest-energy monolayer polymorph and lies below fluorite-type bulk TiF_2 at the PBE level [26]. Bulk TiF_2 itself, however, is thermodynamically metastable, has been prepared only under high pressure, and its disproportionation into TiF_3 and Ti is nearly thermoneutral [67]. Whether the monolayers are stable with respect to mixtures of Ti and higher titanium halides therefore cannot be decided from the available data, because the errors of semilocal functionals in fluoride formation energies are comparable to the energy differences involved; for Janus TiFBr, decomposition into TiF_2 and $TiBr_2$ and conversion into other polytypes must also be considered. A convex-hull analysis with corrected formation energies, which we have not performed, is needed to settle these questions. Possible synthesis routes are suggested by related systems. $TiCl_2$, $TiBr_2$ and TiI_2 exist as layered bulk compounds [16], and transition-metal dihalide layers down to the

monolayer limit have been grown by vapour deposition and epitaxy [68,69]. Janus TMD monolayers have been obtained by replacing one chalcogen layer of a parent monolayer, either at elevated temperature [70,71] or at room temperature with reactive radical precursors [72]; an analogous partial fluorination of a $TiBr_2$ monolayer could in principle yield TiFBr. Fluorination of 2D materials with XeF_2 is established for graphene [73], but such fluorinating agents are corrosive, attack Si-based substrates [73] and are likely to oxidise Ti^{2+} further, so controlling the depth and selectivity of fluorination remains a key challenge.

Chemical stability in water is the most serious open question. Titanium in both layers is formally Ti^{2+}, which is strongly reducing: aqueous Ti(II) is readily oxidised and reduces water [74], so bare Ti^{2+} layers are expected to be prone to oxidation in water. Related Ti-based 2D materials also degrade in water; $Ti_3C_2T_x$ MXenes, for instance, hydrolyse to TiO_2 even in the absence of dissolved O_2 [75]. ≡Ti–F groups on TiO_2 surfaces persist under acidic conditions, with maximal fluorination near pH 3, and are replaced by hydroxyl groups in basic media [76,77]; by analogy, the F-terminated surfaces might offer some kinetic protection in acidic electrolytes, whereas hydroxide exchange would accelerate degradation in neutral and alkaline media, where the TiFBr window lies. Under illumination, holes in the narrow Ti 3d valence band could oxidise Ti^{2+} to Ti^{3+}, which may contribute to photocorrosion and hinder hole transfer to water; this mechanism was not evaluated here. Practical use would therefore require protection strategies demonstrated for unstable 2D crystals and photoelectrodes, such as encapsulation in hexagonal boron nitride [78] or thin protective oxide overlayers [79], designed so that water can still reach the catalytically active sites. Since Ti^{2+} can also release H_2 stoichiometrically through corrosion, experimental tests should distinguish photocatalytic from corrosion-derived hydrogen, for example by showing H_2 evolution well beyond the amount attributable to corrosion of the Ti^{2+} present, sustained activity, post-reaction characterisation and, for overall water splitting, the expected 2:1 H_2:O_2 stoichiometry. A quantitative assessment of photocorrosion, for instance through the thermodynamic oxidation and reduction potentials of the layers [80], is left for future work.

Finally, the present assessment concerns the intrinsic properties of the light absorber. The free energies of the HER and OER intermediates (H*, OH*, O*, OOH*) on the F- and Br-terminated faces and on defect sites were not computed. For the related 1H-$TiBr_2$ monolayer, the pristine basal plane binds H and O only weakly, whereas halogen vacancies create strong chemisorption sites [22]; the catalytically active sites of TiF_2 and TiFBr are therefore likely to involve defects, edges or cocatalysts, as in the most efficient particulate photocatalysts [8,9]. A computational-hydrogen-electrode study of such sites [81,82] is required to assess their catalytic activity. Excitonic effects were also not included. Exciton binding energies of several tenths of an electronvolt are typical of 1H dihalides and dichalcogenides, for example about 0.56 eV calculated for free-standing 1H-$TiBr_2$ [21] and 0.32 eV measured for WS_2 on SiO_2 [83]; they can be estimated from the two-dimensional polarisability and the carrier effective masses [84], while the influence of aqueous dielectric screening on exciton binding in these monolayers remains to be quantified. Efficient exciton dissociation is therefore expected to depend mainly on interfaces with cocatalysts or other semiconductors. Carrier mobilities, which require deformation-potential or electron–phonon calculations, were likewise not evaluated, and heterostructures, including a combination of TiF_2 and TiFBr, were not modelled; the 13% lattice mismatch between the two monolayers would require large commensurate supercells.

4. Conclusions

TiF_2 and Janus TiFBr monolayers were studied with density functional theory to assess their potential as photocatalysts for solar-driven water splitting. Both adopt the trigonal-prismatic 1H structure (space groups P-6m2 and P3m1), satisfy the elastic stability criteria and retain their structure during 10 ps MLFF-MD runs at 300 K in vacuum, and their phonon spectra are consistent with dynamical stability apart from small residual imaginary ZA frequencies near Γ; for TiF_2, the 1H phase is also the lowest-energy monolayer polymorph. At the HSE06 level, TiF_2 has an indirect gap of 2.08 eV and TiFBr a direct gap of 1.45 eV, both of d–d character.

The band edges of TiF_2 straddle the water redox potentials from pH 0 to 9.0 and those of TiFBr from pH 6.4 to 10.2 (a window that a dipole correction might move by roughly 2–4 pH units toward acidic conditions), but these thermodynamic windows shrink once kinetic losses are considered. With overpotential allowances of 0.2 eV for the HER and 0.6 eV for the OER, the band edges of TiF_2 satisfy both allowances only between pH 4.7 and 5.6, where its idealised STH limit reaches 15.8% for complete absorption above the gap, whereas TiFBr lacks the OER driving force for standalone overall water splitting below pH ~ 12. The intrinsic dipole of TiFBr creates a vacuum-level difference between its faces, estimated at 0.95–1.55 eV without a dipole correction, which raises its conduction band on the Br-terminated side and makes TiFBr more suitable for hydrogen evolution than for overall water splitting. After correction to the HSE06 gaps, the main absorption peaks lie at about 2.8 eV for TiF_2 and 1.8 eV for TiFBr, in the blue and the red part of the visible spectrum, respectively; a single TiFBr layer absorbs about twice as many AM1.5G photons as a TiF_2 layer, but each absorbs only 10–12% of the photons above its gap.

Taken together, these results identify TiF_2 as a candidate photocatalyst for overall water splitting under mildly acidic conditions and TiFBr as a candidate for hydrogen evolution whose built-in field raises its conduction band on the Br-terminated side. Their practical use depends on questions that the present study does not resolve and that we regard as priorities for future work: the free energies of reaction intermediates on pristine and defective surfaces, dipole-corrected and heterostructure band alignments, excitonic effects and carrier mobilities, and, above all, the chemical stability of Ti^{2+}-based layers in aqueous electrolytes together with practical routes to their synthesis.

CRediT authorship contribution statement

Bourama Djonfaga: Writing – original draft, Visualization, Investigation, Data curation, Conceptualization. **Murat Sahin:** Writing – review & editing, Resources, Investigation, Conceptualization. **Gokhan Surucu:** Writing – original draft, Validation, Supervision, Software, Methodology, Formal analysis, Conceptualization.

Declaration of Generative AI and AI-Assisted Technologies in the Manuscript Preparation Process

During the preparation of this work, the authors used Claude (Anthropic) in order to improve the language and readability of the manuscript. After using this tool/service, the authors reviewed and edited the content as needed and take full responsibility for the content of the published article.

Declaration of Competing Interest

The authors declare that they have no known competing financial interests or personal relationships that could have appeared to influence the work reported in this paper.

Acknowledgement

The numerical calculations reported in this paper were fully performed at TUBITAK ULAKBIM, High Performance and Grid Computing Center (TRUBA resources).

Appendix A. Supplementary Data

Supplementary data to this article can be found online at https://doi.org/10.1016/j.ijhydene.2026.158609.

References

[1] Chowdhury FA. Recent advances and demonstrated potentials for clean hydrogen via overall solar water splitting. MRS Adv 2019;4:2771–85. https://doi.org/10.1557/adv.2019.444.

[2] Hota P, Das A, Maiti DK. A short review on generation of green fuel hydrogen through water splitting. Int J Hydrogen Energy 2023;48:523–41. https://doi.org/10.1016/j.ijhydene.2022.09.264.

[3] Tentu RD, Basu S. Photocatalytic water splitting for hydrogen production. Curr Opin Electrochem 2017;5:56–62. https://doi.org/10.1016/j.coelec.2017.10.019.

[4] Wang S, Si Y, Lu K, Liu F, Wang B, Zhao S, Wang Y, Zhang S, Lu Y, Li N, Liu M. Energy and mass flow in photocatalytic water splitting by coupling photothermal effect. Chem Phys Rev 2024;5:031301. https://doi.org/10.1063/5.0202991.

[5] Zhao W, Chen H, Zhang J, Low PJ, Sun H. Photocatalytic overall water splitting endowed by modulation of internal and external energy fields. Chem Sci 2024;15:17292–327. https://doi.org/10.1039/D4SC05065G.

[6] Pinaud BA, Benck JD, Seitz LC, Forman AJ, Chen Z, Deutsch TG, James BD, Baum KN, Baum GN, Ardo S, Wang H, Miller E, Jaramillo TF. Technical and economic feasibility of centralized facilities for solar hydrogen production via photocatalysis and photoelectrochemistry. Energy Environ Sci 2013;6:1983–2002. https://doi.org/10.1039/c3ee40831k.

[7] Nishiyama H, Yamada T, Nakabayashi M, Maehara Y, Yamaguchi M, Kuromiya Y, Nagatsuma Y, Tokudome H, Akiyama S, Watanabe T, Narushima R, Okunaka S, Shibata N, Takata T, Hisatomi T, Domen K. Photocatalytic solar hydrogen production from water on a 100-m^2 scale. Nature 2021;598:304–7. https://doi.org/10.1038/s41586-021-03907-3.

[8] Takata T, Jiang J, Sakata Y, Nakabayashi M, Shibata N, Nandal V, Seki K, Hisatomi T, Domen K. Photocatalytic water splitting with a quantum efficiency of almost unity. Nature 2020;581:411–4. https://doi.org/10.1038/s41586-020-2278-9.

[9] Kumar M, Meena B, Subramanyam P, Suryakala D, Subrahmanyam C. Recent trends in photoelectrochemical water splitting: the role of cocatalysts. NPG Asia Mater 2022;14:88. https://doi.org/10.1038/s41427-022-00436-x.

[10] Singh AK, Mathew K, Zhuang HL, Hennig RG. Computational screening of 2D materials for photocatalysis. J Phys Chem Lett 2015;6:1087–98. https://doi.org/10.1021/jz502646d.

[11] Novoselov KS, Geim AK, Morozov SV, Jiang D, Zhang Y, Dubonos SV, Grigorieva IV, Firsov AA. Electric field effect in atomically thin carbon films. Science 2004;306:666–9. https://doi.org/10.1126/science.1102896.

[12] Bhimanapati GR, Lin Z, Meunier V, Jung Y, Cha J, Das S, Xiao D, Son Y, Strano MS, Cooper VR, Liang L, Louie SG, Ringe E, Zhou W, Kim SS, Naik RR, Sumpter BG, Terrones H, Xia F, Wang Y, Zhu J, Akinwande D, Alem N, Schuller JA, Schaak RE, Terrones M, Robinson JA. Recent advances in two-dimensional materials beyond graphene. ACS Nano 2015;9:11509–39. https://doi.org/10.1021/acsnano.5b05556.

[13] Lee J, Kang S, Yim K, Kim KY, Jang HW, Kang Y, Han S. Hydrogen evolution reaction at anion vacancy of two-dimensional transition-metal dichalcogenides: ab initio computational screening. J Phys Chem Lett 2018;9:2049–55. https://doi.org/10.1021/acs.jpclett.8b00712.

[14] Chen J, Tang Q. The versatile electronic, magnetic and photo-electro catalytic activity of a new 2D MA_2Z_4 family. Chem Eur J 2021;27:9925–33. https://doi.org/10.1002/chem.202100851.

[15] Dharma HNC, Jaafar J, Widiastuti N, Matsuyama H, Rajabsadeh S, Othman MHD, Rahman MA, Jafri NNM, Suhaimin NS, Nasir AM, Alias NH. A review of titanium dioxide (TiO_2)-based photocatalyst for oilfield-produced water treatment. Membranes 2022;12:345. https://doi.org/10.3390/membranes12030345.

[16] McGuire MA. Crystal and magnetic structures in layered, transition metal dihalides and trihalides. Crystals 2017;7:121. https://doi.org/10.3390/cryst7050121.

[17] Haastrup S, Strange M, Pandey M, Deilmann T, Schmidt PS, Hinsche NF, Gjerding MN, Torelli D, Larsen PM, Riis-Jensen AC, Gath J, Jacobsen KW, Mortensen JJ, Olsen T, Thygesen KS. The Computational 2D Materials database: high-throughput modeling and discovery of atomically thin crystals. 2D Mater 2018;5:042002. https://doi.org/10.1088/2053-1583/aacfc1.

[18] Gjerding MN, Taghizadeh A, Rasmussen A, Ali S, Bertoldo F, Deilmann T, Knøsgaard NR, Kruse M, Larsen AH, Manti S, Pedersen TG, Petralanda U, Skovhus T, Svendsen MK, Mortensen JJ, Olsen T, Thygesen KS. Recent progress of the Computational 2D Materials database (C2DB). 2D Mater 2021;8:044002. https://doi.org/10.1088/2053-1583/ac1059.

[19] Li X, Zhang Z, Zhang H. High throughput study on magnetic ground states with Hubbard U corrections in transition metal dihalide monolayers. Nanoscale Adv 2020;2:495–501. https://doi.org/10.1039/c9na00588a.

[20] Georgescu AB, Millis AJ, Rondinelli JM. Trigonal symmetry breaking and its electronic effects in the two-dimensional dihalides MX_2 and trihalides MX_3. Phys Rev B 2022;105:245153. https://doi.org/10.1103/PhysRevB.105.245153.

[21] Batista ALO, Palheta JMT, Piotrowski MJ, Rêgo CRC, Guedes-Sobrinho D, Dias AC. Promising TMDC-like optical and excitonic properties of the $TiBr_2$ 2H monolayer. Dalton Trans 2024;53:746–52. https://doi.org/10.1039/d3dt03133k.

[22] Batista ALO, Palheta JMT, Santos EJA, Bastos CMO, Ribeiro Júnior LA, Guedes-Sobrinho D, Rêgo CRC, Piotrowski MJ, Dias AC. Vacancies and adatoms unlock reactivity in 2H-$TiBr_2$ monolayers. Phys Rev Mater 2026;10:034004. https://doi.org/10.1103/qmhs-x85x.

[23] Fischer F, Nielsen CEM, Prada M, Bester G. Unconventional bright ground-state excitons in monolayer TiI_2 from first-principles calculations. npj 2D Mater Appl 2026;10:19. https://doi.org/10.1038/s41699-025-00656-z.

[24] Wang Y, Wei W, Wang H, Mao N, Li F, Huang B, Dai Y. Janus TiXY monolayers with tunable Berry curvature. J Phys Chem Lett 2019;10:7426–32. https://doi.org/10.1021/acs.jpclett.9b02853.

[25] Yang Q, Zhang T, Hu CE, Chen XR, Geng HY. A first-principles study on the electronic, piezoelectric, and optical properties and strain-dependent carrier mobility of Janus TiXY (X ≠ Y, X/Y = Cl, Br, I) monolayers. Phys Chem Chem Phys 2023;25:274–85. https://doi.org/10.1039/d2cp03973g.

[26] Ono S, Pawar R. Fluorite-type materials in the monolayer limit. Phys Rev Mater 2024;8:094002. https://doi.org/10.1103/PhysRevMaterials.8.094002.

[27] Lin S, Shen J, Xiong R, Zhang Y, Chen L, Wen C, Sa B. Theoretically designing polar van der Waals heterostructures for photocatalytic overall water splitting. Phys Chem Chem Phys 2026;28:3099–108. https://doi.org/10.1039/D5CP04252F.

[28] Wang J, Lu J, Zhao X, Hu G, Yuan X, Ren J. Two-dimensional Janus AsXY (X = Se, Te; Y = Br, I) monolayers for photocatalytic water splitting. Eur Phys J B 2023;96:17. https://doi.org/10.1140/epjb/s10051-023-00486-2.

[29] Riis-Jensen AC, Deilmann T, Olsen T, Thygesen KS. Classifying the electronic and optical properties of Janus monolayers. ACS Nano 2019;13:13354–64. https://doi.org/10.1021/acsnano.9b06698.

[30] Li X, Li Z, Yang J. Proposed photosynthesis method for producing hydrogen from dissociated water molecules using incident near-infrared light. Phys Rev Lett 2014;112:018301. https://doi.org/10.1103/PhysRevLett.112.018301.

[31] Fu CF, Sun J, Luo Q, Li X, Hu W, Yang J. Intrinsic electric fields in two-dimensional materials boost the solar-to-hydrogen efficiency for photocatalytic water splitting. Nano Lett 2018;18:6312–7. https://doi.org/10.1021/acs.nanolett.8b02561.

[32] Kresse G, Furthmüller J. Efficiency of ab-initio total energy calculations for metals and semiconductors using a plane-wave basis set. Comput Mater Sci 1996;6:15–50. https://doi.org/10.1016/0927-0256(96)00008-0.

[33] Kresse G, Furthmüller J. Efficient iterative schemes for ab initio total-energy calculations using a plane-wave basis set. Phys Rev B 1996;54:11169–86. https://doi.org/10.1103/PhysRevB.54.11169.

[34] Perdew JP, Burke K, Ernzerhof M. Generalized gradient approximation made simple. Phys Rev Lett 1996;77:3865–8. https://doi.org/10.1103/PhysRevLett.77.3865.

[35] Kresse G, Joubert D. From ultrasoft pseudopotentials to the projector augmented-wave method. Phys Rev B 1999;59:1758–75. https://doi.org/10.1103/PhysRevB.59.1758.

[36] Blöchl PE. Projector augmented-wave method. Phys Rev B 1994;50:17953–79. https://doi.org/10.1103/PhysRevB.50.17953.

[37] Liu ZL, Ekuma CE, Li WQ, Yang JQ, Li XJ. ElasTool: an automated toolkit for elastic constants calculation. Comput Phys Commun 2022;270:108180. https://doi.org/10.1016/j.cpc.2021.108180.

[38] Kastuar SM, Ekuma CE, Liu ZL. Efficient prediction of temperature-dependent elastic and mechanical properties of 2D materials. Sci Rep 2022;12:3776. https://doi.org/10.1038/s41598-022-07819-8.

[39] Togo A. First-principles phonon calculations with phonopy and phono3py. J Phys Soc Jpn 2023;92:012001. https://doi.org/10.7566/JPSJ.92.012001.

[40] Togo A, Chaput L, Tadano T, Tanaka I. Implementation strategies in phonopy and phono3py. J Phys Condens Matter 2023;35:353001. https://doi.org/10.1088/1361-648X/acd831.

[41] Jinnouchi R, Karsai F, Kresse G. On-the-fly machine learning force field generation: application to melting points. Phys Rev B 2019;100:014105. https://doi.org/10.1103/PhysRevB.100.014105.

[42] Jinnouchi R, Lahnsteiner J, Karsai F, Kresse G, Bokdam M. Phase transitions of hybrid perovskites simulated by machine-learning force fields trained on the fly with Bayesian inference. Phys Rev Lett 2019;122:225701. https://doi.org/10.1103/PhysRevLett.122.225701.

[43] Heyd J, Scuseria GE, Ernzerhof M. Hybrid functionals based on a screened Coulomb potential. J Chem Phys 2003;118:8207–15. https://doi.org/10.1063/1.1564060.

[44] Krukau AV, Vydrov OA, Izmaylov AF, Scuseria GE. Influence of the exchange screening parameter on the performance of screened hybrid functionals. J Chem Phys 2006;125:224106. https://doi.org/10.1063/1.2404663.

[45] Ganose AM, Jackson AJ, Scanlon DO. Sumo: command-line tools for plotting and analysis of periodic ab initio calculations. J Open Source Softw 2018;3:717. https://doi.org/10.21105/joss.00717.

[46] Momma K, Izumi F. VESTA 3 for three-dimensional visualization of crystal, volumetric and morphology data. J Appl Crystallogr 2011;44:1272–6. https://doi.org/10.1107/S0021889811038970.

[47] Gajdoš M, Hummer K, Kresse G, Furthmüller J, Bechstedt F. Linear optical properties in the projector-augmented wave methodology. Phys Rev B 2006;73:045112. https://doi.org/10.1103/PhysRevB.73.045112.

[48] Wang V, Xu N, Liu JC, Tang G, Geng WT. VASPKIT: a user-friendly interface facilitating high-throughput computing and analysis using VASP code. Comput Phys Commun 2021;267:108033. https://doi.org/10.1016/j.cpc.2021.108033.

[49] Li Y, Heinz TF. Two-dimensional models for the optical response of thin films. 2D Mater 2018;5:025021. https://doi.org/10.1088/2053-1583/aab0cf.

[50] Levine ZH, Allan DC. Linear optical response in silicon and germanium including self-energy effects. Phys Rev Lett 1989;63:1719–22. https://doi.org/10.1103/PhysRevLett.63.1719.

[51] Del Sole R, Girlanda R. Optical properties of semiconductors within the independent-quasiparticle approximation. Phys Rev B 1993;48:11789–95. https://doi.org/10.1103/PhysRevB.48.11789.
[52] Haman Z, Kibbou M, Khossossi N, Ouabida E, Dey P, Essaoudi I, Ainane A. Harnessing intrinsic electric fields in 2D Janus MoOX (X = S, Se, and Te) monolayers for enhanced photocatalytic hydrogen evolution. Int J Hydrogen Energy 2024;68:566–74. https://doi.org/10.1016/j.ijhydene.2024.04.257.
[53] ASTM G173-03. Standard tables for reference solar spectral irradiances: direct normal and hemispherical on 37° tilted surface. West Conshohocken (PA): ASTM International; 2020. https://doi.org/10.1520/G0173-03R20. 2020.
[54] Cordero B, Gómez V, Platero-Prats AE, Revés M, Echeverría J, Cremades E, Barragán F, Alvarez S. Covalent radii revisited. Dalton Trans 2008:2832–8. https://doi.org/10.1039/B801115J.
[55] Born M, Huang K. Dynamical theory of crystal lattices. Oxford: Clarendon Press; 1954.
[56] Carrete J, Li W, Lindsay L, Broido DA, Gallego LJ, Mingo N. Physically founded phonon dispersions of few-layer materials and the case of borophene. Mater Res Lett 2016;4:204–11. https://doi.org/10.1080/21663831.2016.1174163.
[57] Lin C, Poncé S, Marzari N. General invariance and equilibrium conditions for lattice dynamics in 1D, 2D, and 3D materials. npj Comput Mater 2022;8:236. https://doi.org/10.1038/s41524-022-00920-6.
[58] Yuan G, Ma X, Liao J, Xie T, Xie Q, Yuan Z. First-principles calculations of 2D Janus $WSSiN_2$ monolayer for photocatalytic water splitting. ACS Appl Nano Mater 2023;6:1956–64. https://doi.org/10.1021/acsanm.2c04918.
[59] Abyaz B, Mahdavifar Z, Schreckenbach G. 2D $Mg_2M_2X_5$ (M = B, Al, Ga, In, Tl; X = S, Se, Te) monolayers: novel stable semiconductors for water splitting photocatalysts. Appl Surf Sci 2023;621:156892. https://doi.org/10.1016/j.apsusc.2023.156892.
[60] Yu Y, Zhou J, Guo Z, Sun Z. Novel two-dimensional Janus $MoSiGeN_4$ and $WSiGeN_4$ as highly efficient photocatalysts for spontaneous overall water splitting. ACS Appl Mater Interfaces 2021;13:28090–7. https://doi.org/10.1021/acsami.1c04138.
[61] Himmet F, Surucu G, Lisesivdin SB, Surucu O, Altuntas G, Bostan B, Gencer A. Innovative 2D materials for efficient photocatalysis: a comparative study for WSi_2N_4, WGe_2N_4, and their Janus counterpart $WSiGeN_4$ monolayers. Int J Hydrogen Energy 2024;78:761–72. https://doi.org/10.1016/j.ijhydene.2024.06.304.
[62] Neugebauer J, Scheffler M. Adsorbate-substrate and adsorbate-adsorbate interactions of Na and K adlayers on Al(111). Phys Rev B 1992;46:16067–80. https://doi.org/10.1103/PhysRevB.46.16067.
[63] Bengtsson L. Dipole correction for surface supercell calculations. Phys Rev B 1999;59:12301–4. https://doi.org/10.1103/PhysRevB.59.12301.
[64] Trasatti S. The absolute electrode potential: an explanatory note (recommendations 1986). Pure Appl Chem 1986;58:955–66. https://doi.org/10.1351/pac198658070955.
[65] Bernardi M, Palummo M, Grossman JC. Extraordinary sunlight absorption and one nanometer thick photovoltaics using two-dimensional monolayer materials. Nano Lett 2013;13:3664–70. https://doi.org/10.1021/nl401544y.
[66] Xu Q, Zhang L, Yu J, Wageh S, Al-Ghamdi AA, Jaroniec M. Direct Z-scheme photocatalysts: principles, synthesis, and applications. Mater Today 2018;21:1042–63. https://doi.org/10.1016/j.mattod.2018.04.008.
[67] Nikitin MI, Osina EL, Alikhanyan AS. Revisiting the thermodynamic characteristics of titanium fluorides. Russ J Inorg Chem 2023;68:278–86. https://doi.org/10.1134/S003602362260280X.
[68] Liu H, Wang X, Wu J, Chen Y, Wan J, Wen R, Yang J, Liu Y, Song Z, Xie L. Vapor deposition of magnetic van der Waals NiI_2 crystals. ACS Nano 2020;14:10544–51. https://doi.org/10.1021/acsnano.0c04499.
[69] Hadjadj SE, González-Orellana C, Lawrence J, Bikaljević D, Peña-Díaz M, Gargiani P, Aballe L, Naumann J, Niño MÁ, Foerster M, Ruiz-Gómez S, Thakur S, Kumberg I, Taylor JM, Hayes J, Torres J, Luo C, Radu F, de Oteyza DG, Kuch W, Pascual JI, Rogero C, Ilyn M. Epitaxial monolayers of the magnetic 2D semiconductor $FeBr_2$ grown on Au(111). Chem Mater 2023;35:9847–56. https://doi.org/10.1021/acs.chemmater.3c00978.
[70] Lu AY, Zhu H, Xiao J, Chuu CP, Han Y, Chiu MH, Cheng CC, Yang CW, Wei KH, Yang Y, Wang Y, Sokaras D, Nordlund D, Yang P, Muller DA, Chou MY, Zhang X, Li LJ. Janus monolayers of transition metal dichalcogenides. Nat Nanotechnol 2017;12:744–9. https://doi.org/10.1038/nnano.2017.100.
[71] Zhang J, Jia S, Kholmanov I, Dong L, Er D, Chen W, Guo H, Jin Z, Shenoy VB, Shi L, Lou J. Janus monolayer transition-metal dichalcogenides. ACS Nano 2017;11:8192–8. https://doi.org/10.1021/acsnano.7b03186.
[72] Trivedi DB, Turgut G, Qin Y, Sayyad MY, Hajra D, Howell M, Liu L, Yang S, Patoary NH, Li H, Petrić MM, Meyer M, Kremser M, Barbone M, Soavi G, Stier AV, Müller K, Yang S, Esqueda IS, Zhuang H, Finley JJ, Tongay S. Room-temperature synthesis of 2D Janus crystals and their heterostructures. Adv Mater 2020;32:2006320. https://doi.org/10.1002/adma.202006320.
[73] Nair RR, Ren W, Jalil R, Riaz I, Kravets VG, Britnell L, Blake P, Schedin F, Mayorov AS, Yuan S, Katsnelson MI, Cheng HM, Strupinski W, Bulusheva LG, Okotrub AV, Grigorieva IV, Grigorenko AN, Novoselov KS, Geim AK. Fluorographene: a two-dimensional counterpart of Teflon. Small 2010;6:2877–84. https://doi.org/10.1002/smll.201001555.
[74] Dhar BB, Gould ES. Hypovalent titanium and Ti(II)–Ti(III) interconversions. Dalton Trans 2010;39:1616–9. https://doi.org/10.1039/b914989a.
[75] Huang S, Mochalin VN. Hydrolysis of 2D transition-metal carbides (MXenes) in colloidal solutions. Inorg Chem 2019;58:1958–66. https://doi.org/10.1021/acs.inorgchem.8b02890.
[76] Park H, Choi W. Effects of TiO_2 surface fluorination on photocatalytic reactions and photoelectrochemical behaviors. J Phys Chem B 2004;108:4086–93. https://doi.org/10.1021/jp036735i.
[77] Minella M, Faga MG, Maurino V, Minero C, Pelizzetti E, Coluccia S, Martra G. Effect of fluorination on the surface properties of titania P25 powder: an FTIR study. Langmuir 2010;26:2521–7. https://doi.org/10.1021/la902807g.
[78] Cao Y, Mishchenko A, Yu GL, Khestanova E, Rooney AP, Prestat E, Kretinin AV, Blake P, Shalom MB, Woods C, Chapman J, Balakrishnan G, Grigorieva IV, Novoselov KS, Piot BA, Potemski M, Watanabe K, Taniguchi T, Haigh SJ, Geim AK, Gorbachev RV. Quality heterostructures from two-dimensional crystals unstable in air by their assembly in inert atmosphere. Nano Lett 2015;15:4914–21. https://doi.org/10.1021/acs.nanolett.5b00648.
[79] Hu S, Shaner MR, Beardslee JA, Lichterman M, Brunschwig BS, Lewis NS. Amorphous TiO_2 coatings stabilize Si, GaAs, and GaP photoanodes for efficient water oxidation. Science 2014;344:1005–9. https://doi.org/10.1126/science.1251428.
[80] Chen S, Wang LW. Thermodynamic oxidation and reduction potentials of photocatalytic semiconductors in aqueous solution. Chem Mater 2012;24:3659–66. https://doi.org/10.1021/cm302533s.
[81] Nørskov JK, Rossmeisl J, Logadottir A, Lindqvist L, Kitchin JR, Bligaard T, Jónsson H. Origin of the overpotential for oxygen reduction at a fuel-cell cathode. J Phys Chem B 2004;108:17886–92. https://doi.org/10.1021/jp047349j.
[82] Rossmeisl J, Qu ZW, Zhu H, Kroes GJ, Nørskov JK. Electrolysis of water on oxide surfaces. J Electroanal Chem 2007;607:83–9. https://doi.org/10.1016/j.jelechem.2006.11.008.
[83] Chernikov A, Berkelbach TC, Hill HM, Rigosi A, Li Y, Aslan OB, Reichman DR, Hybertsen MS, Heinz TF. Exciton binding energy and nonhydrogenic Rydberg series in monolayer WS_2. Phys Rev Lett 2014;113:076802. https://doi.org/10.1103/PhysRevLett.113.076802.
[84] Olsen T, Latini S, Rasmussen F, Thygesen KS. Simple screened hydrogen model of excitons in two-dimensional materials. Phys Rev Lett 2016;116:056401. https://doi.org/10.1103/PhysRevLett.116.056401.